Correspondence to:
A. Verdy,
averdy@ucsd.edu

Balancing Volume, Temperature, and Salinity Budgets During 2014–2018 in the Tropical Pacific Ocean State Estimate

Ariane Verdy[1] ⓘ, Matthew R. Mazloff[1] ⓘ, Bruce D. Cornuelle[1] ⓘ, and Aneesh C. Subramanian[2] ⓘ

[1]Scripps Institution of Oceanography, University of California, San Diego, La Jolla, CA, USA, [2]Atmospheric and Oceanic Sciences, Colorado University, Boulder, CO, USA

Abstract A state estimate of the tropical Pacific Ocean is used to analyze regional volume, temperature, and salinity budgets during 2014–2018. The simulated ocean state is constrained by both model dynamics and assimilated observations. Comparisons with independent mooring data show that the state estimate is consistent with the observed variability in temperature and velocity. Budgets are analyzed between 5°S and 5°N in the upper 300 m, inside a box defined to represent the central and eastern equatorial Pacific. Transports through the faces of this box are quantified to understand the processes responsible for variability in box-mean properties. Vertical mixing across 300 m is negligible; temperature and salinity tendencies are balanced by surface fluxes and advective divergence, which is decomposed into geostrophic and ageostrophic components. The onset and recovery of the 2015/2016 El Niño event is found to be dominated by anomalous surface fluxes and horizontal advection. During the onset phase, weaker trade winds cause the shallow meridional overturning circulation to slow down, which reduces the poleward transport of heat and leads to upper ocean warming. Anomalous precipitation and advection of fresh water from the western Pacific drive the net freshening of the region. Relaxation from El Niño conditions is dominated by wind-driven meridional advection at 5°N. As the meridional advection regains strength, Ekman advection efficiently exports the warm, fresh surface water out of the equatorial region. Quantifying the heat and salt transport changes in response to wind variability strengthens our understanding of global ocean heat transport.

Plain Language Summary We have combined observations and an ocean model to produce an estimate of the tropical Pacific Ocean properties. Of particular interest are changes to the upper-ocean temperature and salinity over the period 2014–2018. The largest changes occur in the central and eastern equatorial Pacific, and to diagnose the causes we define an analysis box representative of that region. Transports through five faces of this box (the sixth face is a land boundary) are diagnosed to understand the processes responsible for variability in box-average properties. We examine the cooling and freshening that occurs during the El Niño event of 2015/2016. The region is typically characterized by a near surface poleward flow away from the equator and a compensating flow toward the equator from below. This circulation is wind driven and slows down due to changing winds associated with the El Niño. When the winds return to their average state, currents are re-invigorated, leading to the dissipation of El Niño conditions. This paper focuses on determining the size and timing of these processes.

1. Introduction

Balancing the volume, heat, and salt budgets in the equatorial Pacific Ocean is critical for understanding interannual variability in the upper ocean, which is dominated by the El Niño-Southern Oscillation (ENSO). Dubbed the "Wyrtki Challenge," the problem of quantifying the contributions of upwelling, horizontal transport, and surface fluxes to regional budgets was originally proposed by Wyrtki (1981) and remains a priority for the Tropical Pacific Observing System (TPOS; Cravatte et al., 2016). A recent data-assimilation product, the Tropical Pacific Ocean State Estimate (TPOSE; Verdy et al., 2017), provides an opportunity to address this challenge.

Heat export from the tropical Pacific is a leading signal in global ocean heat transport (OHT; Forget & Ferreira, 2011); the result of wind-driven thermocline gyres (Ferrari & Ferreira, 2011), it dominates the equatorial upper ocean heat budget interannual variability (Roberts et al., 2017). In the tropical Pacific, wind-driven meridional Ekman transport divergence of surface waters is balanced by upwelling and geostrophic transport convergence, leading to shallow meridional overturning cells (Capotondi et al., 2005; Johnson et al., 2001; Perez & Kessler, 2009). These circulation patterns change during El Niño as a result of wind changes (Izumo, 2005;

Song et al., 2018). In addition, the Western Pacific Warm Pool, where sea surface temperature exceeds 28°C and sea surface salinity is less than 35 psu, migrates eastward during El Niño (Kim et al., 2012; McPhaden et al., 2006), which influences local atmospheric convection as part of the Bjerknes feedback. Decrease in tropical Pacific Ocean heat content during El Niño (Cheng et al., 2019) also has implications for OHT variability.

Heat budgets can be useful for identifying the dominant physical mechanisms involved in the onset and recovery of El Niño events. Warm Water Volume (WWV), defined by temperatures above 20°C in the region 120°E–80°W, 5°N–5°S, is a key metric in ENSO prediction (Meinen & McPhaden, 2000); understanding the individual processes controlling its variability is critical for improving El Niño forecasting. In an idealized modeling study, Huguenin et al. (2020) quantified the adiabatic and diabatic processes affecting WWV during El Niños and La Niñas, highlighting the asymmetry between the two phases even with symmetric forcing. Real-life El Niños, with their inherent diversity, are classified as either East-Pacific or Central-Pacific (also referred to as Modoki) of type I or type II. Based on heat budgets constructed from monthly observational data products in the Niño4 region, Wang et al. (2019) and Guan et al. (2023) compare the development of the two types of Central-Pacific El Niños; they find that zonal advection dominates the balance during the onset of type I events, whereas vertical advection dominates during type II events.

In this paper, we quantify the budgets in TPOSE during 2014–2018, which includes one El Niño and two La Niña events. We present a detailed analysis of the contributions of geostrophic and ageostrophic horizontal advection, vertical advection, and surface forcing to the development of temperature and salinity anomalies. Our results highlight interannual variability in the various branches of the shallow meridional overturning circulation and in the associated transports of heat and salt. The bulk of our analysis focuses on the basin-scale evolution of ocean properties between 5°N and 5°S in the top 300 m. In that respect, it offers a model-based counterpart to the recent observational analysis of Kessler et al. (2019), who estimated interannual variability in the meridional temperature advection into the equatorial Pacific during 2008–2015; using a combination of glider transects and mapped observational products, they find that surface divergence accounts for most of the interannual variability in regional temperature tendency. Our analysis explores how this meridional divergence and other terms in the temperature and salinity balances change during the 2015/2016 El Niño.

Several thorough and detailed discussions of the 2015/2016 El Niño and its context are available. This was not a typical El Niño (Xie & Fang, 2020); its signature was large in Niño4 and Niño3.4 indices, but relatively weak in Niño3 and Niño1+2 in the east (Santoso et al., 2017). L'Heureux et al. (2017) show surface and subsurface evolution, and discuss the predictions and mechanisms. The present study addresses the basin-scale variability during this particular event; other El Niños might have very different temperature and salinity balances. An extension of the work could further examine the spatial patterns in the processes at play, which are critical in defining the different types of El Niño events.

The state estimate analyzed here is a model-observations synthesis produced by constraining a regional setup of the MIT general circulation model to fit data from Argo floats, hydrography, and satellites through the adjoint method (4D-Var), resulting in a dynamically consistent estimate of the ocean state. The original TPOSE product described in Verdy et al. (2017) has been extended to cover the period 2010–2018. Details on the data assimilation framework, which employs the methodology from ECCO (consortium for Estimating the Circulation and Climate of the Ocean; Wunsch and Heimbach, 2013), are given in Section 2. The regional state estimate is skilled at reproducing independent observations, such as velocity measurements from the Tropical Atmosphere Ocean/Triangle Trans-Ocean Buoy Network (TAO/TRITON) mooring array (http://www.pmel.noaa.gov/tao/). TPOSE outperforms the global ECCO state estimate (Forget et al., 2015) in fitting observed velocities; the mean currents are better captured in part because equatorial Pacific data are a relatively small constraint in the global setup, and the variability is better simulated because ECCO does not aim to reproduce the location and timing of eddies and waves (only their statistics). Zonal currents are known to exhibit large changes associated with ENSO; this variability, as well as changes in upper ocean temperature and salinity, are captured in TPOSE and described in Section 3. The budget analyses are presented in Section 4. In Section 5, results are discussed and a quantitative assessment of the primary contributions to variability during the 2015/2016 El Niño is presented. Concluding remarks are given in Section 6.
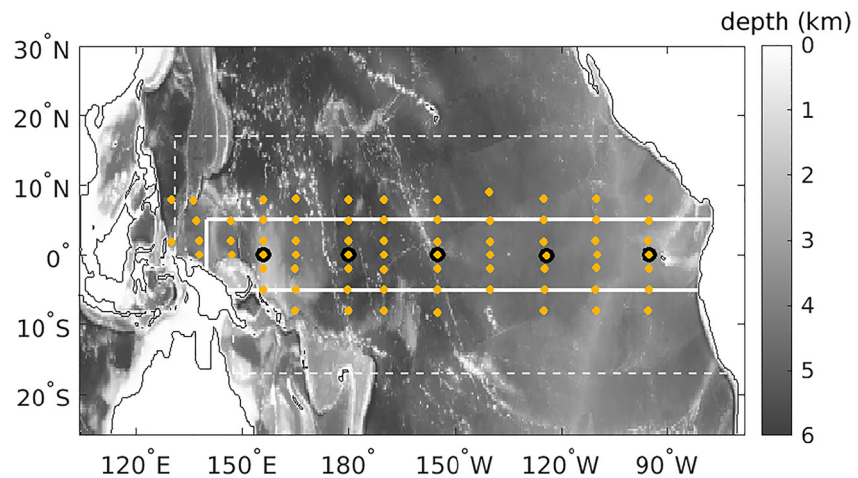
Figure 1. Model domain and bathymetry. Dashed white lines bound the region in which observations were assimilated. The analysis focuses on the region inside the solid white box. TAO/ moorings are shown as orange markers, with black circles around the moorings that were used for the plots in Figure 5.

2. Methods

2.1. Tropical Pacific Ocean State Estimate (TPOSE)

TPOSE is a regional hindcast of the tropical Pacific Ocean between 26°S and 30°N (Figure 1). It is produced using the software from ECCO (Wunsch & Heimbach, 2013) to implement the adjoint method, also known as four-dimensional variational method (4D-Var). It estimates the state of the ocean by optimizing temperature and salinity initial conditions and the atmospheric exchanges of momentum, heat, and freshwater in order to bring the model solution into consistency with assimilated TPOS data sets. After making adjustments to initial conditions and forcing fields, the model governing equations are solved without additional corrections; the result is a free model run with closed dynamical and thermodynamic budgets, allowing the study of governing physics.

The ocean model is a configuration of the Massachusetts Institute of Technology General Circulation Model (MITgcm; Marshall et al., 1997) with a resolution of 1/3° and 51 vertical levels with thickness increasing with depth from 5 m near the surface. The governing equations are stepped forward with a 30-min time step. Lateral open-ocean boundary conditions are obtained from the global reanalysis of the Hybrid Coordinate Ocean Model with Navy Coupled Ocean Data Assimilation (HYCOM/NCODA; http://hycom.org) and prescribed every 5 days. Vertical mixing is parameterized by the K-profile parameterization (KPP) formulation of Large et al. (1994); mixing parameter values are given in Table 1 of Verdy et al. (2017).

Observational constraints come from Argo profiling floats (Argo, 2000), shipborne conductivity temperature and depth (CTD) and expendable bathythermograph (XBT) profiles from the World Ocean Database (WOD18; Boyer et al., 2018), along-track altimetry from the Radar Altimetry Database System (RADS; Scharroo et al., 2013), and optimally interpolated microwave sea surface temperature (MW OI SST) from Remote Sensing Systems (http://www.remss.com/). Only observations in the region from 17°S to 17°N and east of 130°E are used as constraints. They are assigned a spatially dependent uncertainty (Verdy et al., 2017). TAO/TRITON mooring data (http://www.pmel.noaa.gov/tao) are used for independent validation.

The TPOSE product is constructed by combining a series of overlapping 4-month state estimates starting 1 January 2010 and every 2 months afterward. The state estimates are merged by adding the overlapping estimates with weights that vary from 1 at the center of the window to 0 at the edges to create a continuous product for 2010–2018; the methodology is illustrated in Figure 2. This is done for each state variable and other diagnostic terms, at each model grid point. The 4-month assimilation window was chosen as it is long enough for observational constraints to propagate information through the domain and influence atmospheric forcing, but short enough that the location and timing of many mesoscale eddies and planetary waves can be captured by adjusting initial conditions and forcing.
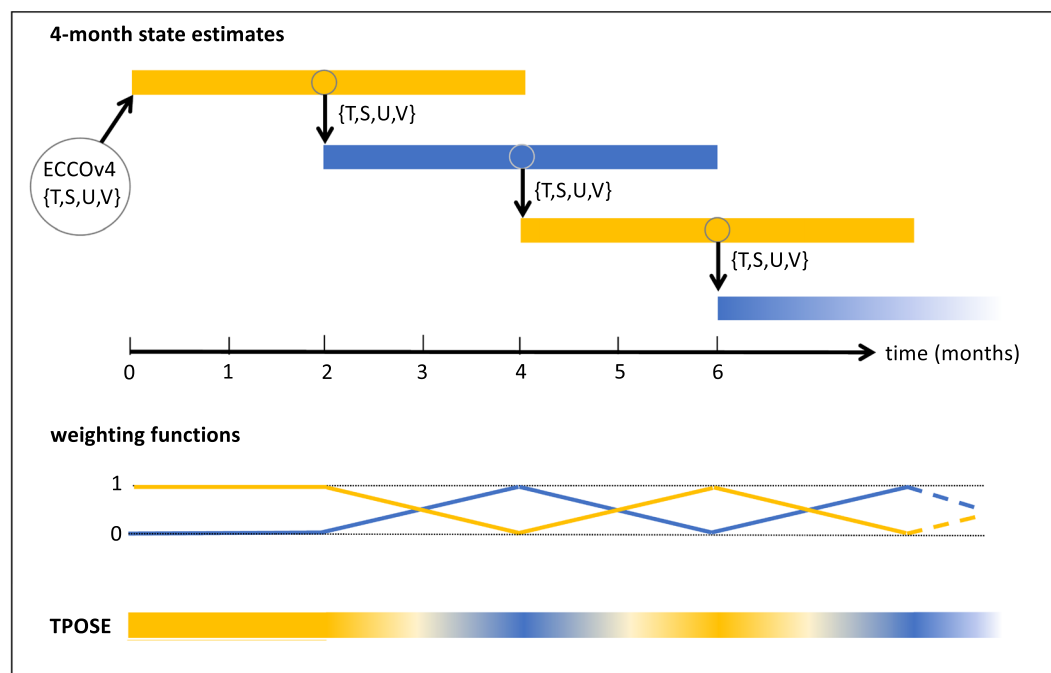
Figure 2. State estimation methodology. 4-month state estimates are staggered by 2 months, and the overlaps are averaged using a linear weighting function to make the TPOSE product. The first state estimate is initialized from ECCOv4 and adjusted through the adjoint to fit observations; subsequent state estimates are initialized from the end of the second month of the previous adjusted 4-month model run. For each state estimate, adjustments are made only to initial conditions (temperature and salinity) and atmospheric state (winds, surface temperature and humidity, rain, shortwave and longwave heat fluxes throughout the 4-month window).

The first 4-month state estimate starting in January 2010 is initialized from the ECCO version 4, release 4 global product (Forget et al., 2015), and each subsequent assimilation is initialized from the previous state estimate. The method goes like this:

1. A 4-month forward model run starts from ECCO initial conditions. The cost function (model–observations misfit) is calculated.
2. The adjoint model is run; control parameters are adjusted to minimize the cost function.
3. A new 4-month forward model run is initialized from the end of the 2nd month of the previous state estimate.
4. The adjoint model is run to optimize the state estimate created in step 3; control parameters are adjusted.
5. Steps 3 and 4 are repeated for each 4-month state estimate.

The goal of the method is not to initialize a forecast, as in numerical weather prediction, but as a hindcast test of the model dynamics and a diagnosis of the mechanisms (Wunsch & Heimbach, 2013). After the adjustment of the control parameters, the model evolves for 4 months without nudging or flux corrections, testing the hypothesis that the model dynamics are adequate to represent the real world (Penny et al., 2019).

The control parameters adjusted through the adjoint method are (a) temperature and salinity initial conditions (at the beginning of each 4-month state estimate), and (b) atmospheric state (wind vector, air temperature, shortwave radiation, and air humidity). They are adjusted through the iterative adjoint process, within assigned uncertainties to prevent overfitting the data. The prior (first-guess) atmospheric state is from the ERA5 reanalysis (Hersbach et al., 2018) starting in 2014, and from the ERA-Interim reanalysis by the European Centre for Medium-Range Weather Forecasts (ECMWF; Dee et al., 2011) before that. Both products are used at their finest temporal resolution, that is, hourly for ERA5 and 6-hourly for ERA-Interim. Adjustments to the prior atmospheric state occur at 10-day intervals. During the model run, atmospheric state variables (as well as open boundary conditions) are linearly interpolated between prescribed values at every time step.
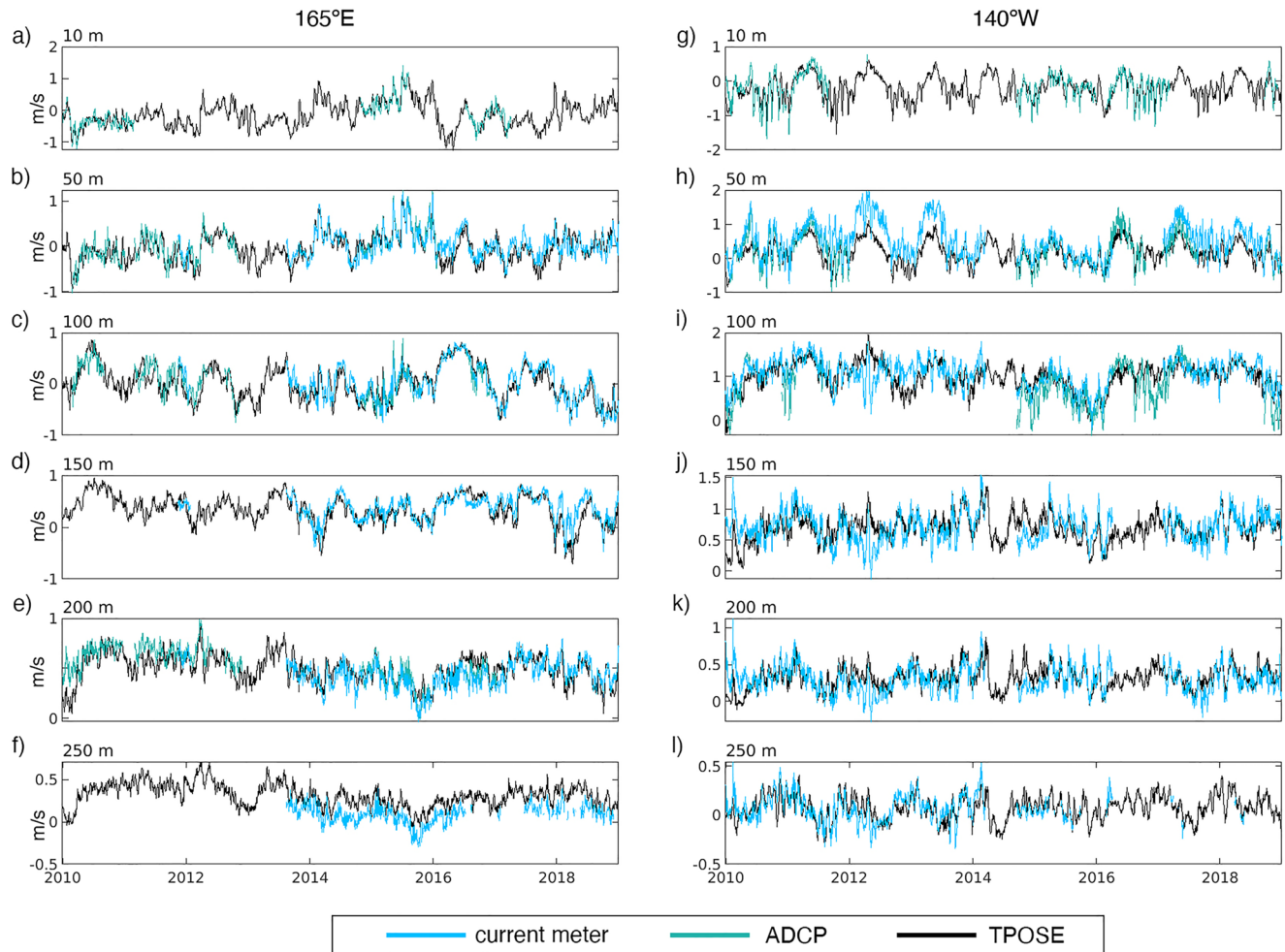
Figure 3. Daily averaged zonal velocity (ms^{-1}) in TPOSE (black) over the years 2010 through 2018 plotted with independent data from TAO/TRITON moorings (blue) at 10, 50, 100, 150, 200, and 250 m depth.

2.2. Validation

The comparison of the state estimate velocities to independent velocity observations in Figures 3 and 4 provide cross-validation. Figure 3 shows the comparison with TAO/TRITON mooring velocities at six depths and two longitudes on the equator. The time series are qualitatively similar, except for some misfits at 250 m at 165°E and at 50 m at 140°W, particularly during 2012 and 2013. These could be due to bias in the state estimate or in the observations; it should be noted that in 2011 the current meter data is not in agreement with the ADCP data at 50 m at the 140°W mooring.

The time mean zonal currents from TPOSE, the global ECCOv4r4 product, and ADCP observations (Johnson et al., 2002) are compared versus latitude at multiple depths for the same two longitudes in Figure 4. The large-scale structure is generally qualitatively similar, although smoother, but there are large differences at 255 m at 165°E and at 205 and 255 m at 140°W. This is likely due to the relatively large viscosity and diffusivity of the model which suppresses the zonal jets at these depths. However, the state estimate does represent a smoothed version of the jets with some fidelity. Near the surface, ECCO and TPOSE zonal currents have similar patterns and magnitudes. However, below ~100 m, the ECCO solution tends to underestimate the EUC. Below ~200 m, it fails to capture the zonal jets. The regional TPOSE product was developed to better simulate some of these features that are not resolved in global state estimates.
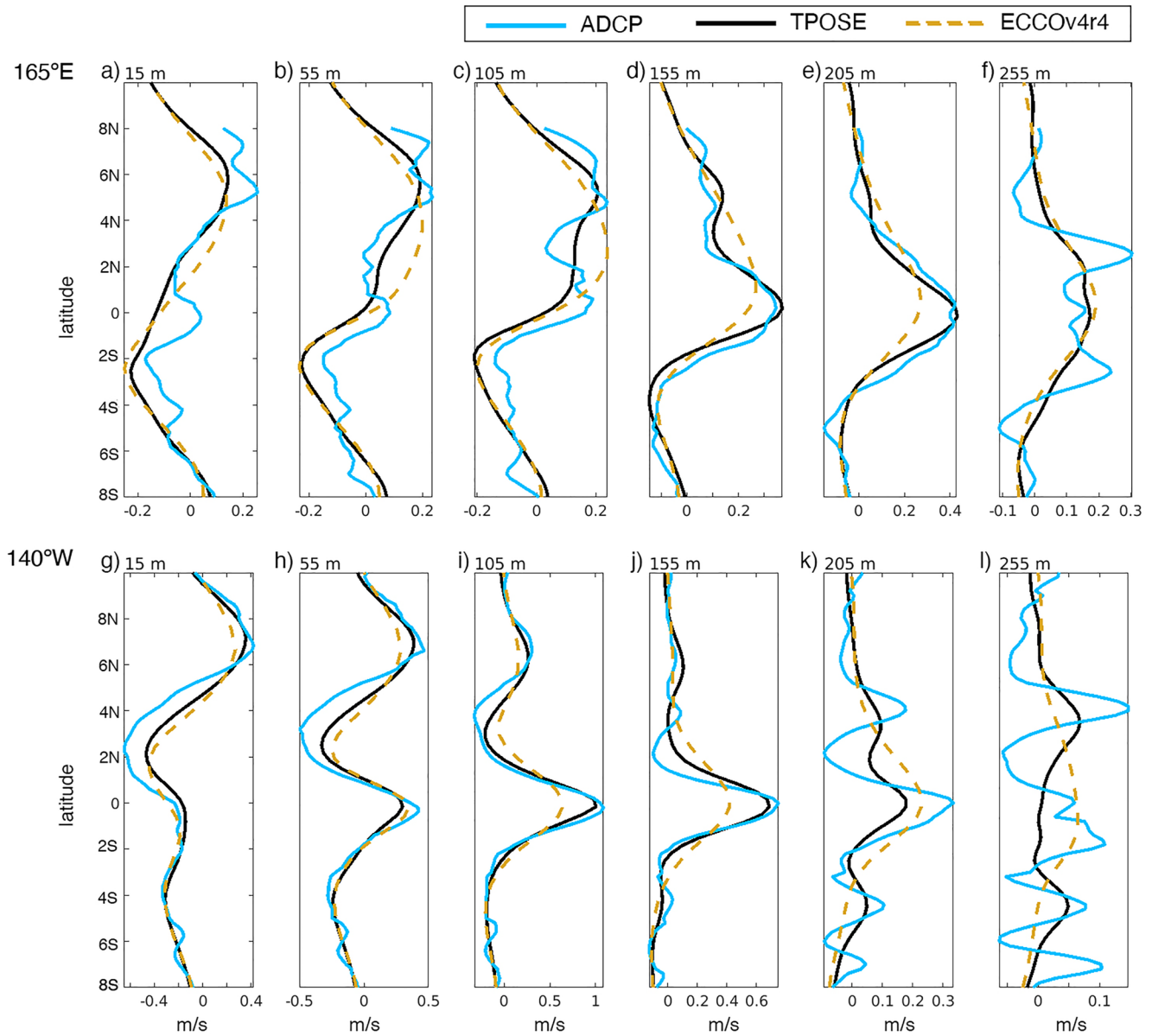
Figure 4. Mean zonal velocity (ms^{-1}) versus latitude in TPOSE (black; 2010–2018), ECCOv4r4 (dashed brown; 2010–2017), and ADCP data (blue; from Johnson et al. (2002)) at different depths. Note that the abscissa scaling varies with depth.

2.3. Budgets

Volume, temperature, and salinity budgets are evaluated for the top 300 m in the region between 5°S and 5°N, east of 140°E, ending at the eastern land boundary. We call this region our "analysis box." The meridional boundaries at ±5° match Wyrtki's analysis domain, which encompasses the upwelling region and the cold tongue and allowed them to infer reasonable calculated values of the Ekman transport (Wyrtki, 1981). The zonal boundaries are set to exclude the maritime continent in the west and avoid boundary transport in the east. We tested moving the western face to 120°E and it did not qualitatively change our findings. The WWV analysis of Huguenin et al. (2020) is done in a similar region, 120°E–80°W and 5°S–5°N. Because they extend farther to the west, their budgets include the Indonesian throughflow. The depth of our box was chosen because the mixing of heat and salt across 300 m is small, both in the mean and time-varying signals, as discussed later.

Budget terms are calculated from daily averaged model diagnostics following the method detailed in Piecuch (2017) to close the budgets exactly for each 4-month state estimate. Solutions from overlapping state estimates are then linearly combined into a multi-year budget (Figure 2). We focus our analysis on the period 2014 through 2018.

The pointwise volume balance is given by

$$\frac{1}{H}\frac{\partial \eta}{\partial t} = -\nabla_h \cdot \vec{v} - \frac{\partial w}{\partial z} + \frac{F}{\rho \Delta z} \tag{1}$$

where H is water column depth, η is sea surface height (SSH), ∇_h is the horizontal gradient, $\vec{v}$ is the horizontal velocity vector, w is vertical velocity, F is the freshwater flux, ρ is density, and Δz is the thickness of the top model layer.

For the temperature budget equation, we adopt the flux form for the advective term as proposed by Lee et al. (2004),

$$\frac{\partial T}{\partial t} = -\nabla_h \cdot \vec{v}(T - T_{\text{ref}}) - \frac{\partial}{\partial z}w(T - T_{\text{ref}}) + \nabla \cdot (\vec{\kappa}_T \cdot \nabla T) + K_T^{turb} + \frac{Q}{\rho C_p \Delta z} \tag{2}$$

where T is potential temperature, T_{ref} is a reference temperature, $\vec{\kappa}$ is the diffusivity, K^{turb} is the KPP turbulent diffusion term (including both vertical diffusion and non-local transport to represent convective mixing), Q is the net air-sea heat flux (defined as positive when into the ocean), and C_p is the specific heat capacity of seawater. When the analysis volume is conserved this budget can be converted into an enthalpy (heat) budget by multiplying by ρC_p (McDougall, 2003), however here we have opted to leave it as a temperature budget.

Similarly, the salinity (S) budget equation is

$$\frac{\partial S}{\partial t} = -\nabla_h \cdot \vec{v}(S - S_{\text{ref}}) - \frac{\partial}{\partial z}w(S - S_{\text{ref}}) + \nabla \cdot (\vec{\kappa}_S \cdot \nabla S) + K_S^{turb} - \frac{F}{\Delta z} \tag{3}$$

where S_{ref} is a reference salinity.

The freshwater and air-sea heat fluxes are calculated in the model from the adjusted ERA5 atmospheric state and the surface ocean state, through the Large and Yeager (2009) bulk formulas.

Integrating Equation 1 over the box gives the budget equation for the regional volume, $\mathcal{V}$:

$$\underbrace{\frac{\partial \mathcal{V}}{\partial t}}_{TEND} = \underbrace{U_{140E} + V_{5S} - V_{5N}}_{ADV_H} + \underbrace{W_{-300m}}_{ADV_V} + \underbrace{\frac{1}{\rho}\iint F \, dx dy}_{SURF} \tag{4}$$

where U, V, and W are the transports (velocity times area) integrated over each face (west face at 140°E, south face at 5°S, north face at 5°N, and bottom face at 300 m).

The volume integrated temperature and salinity budget equations are

$$\underbrace{\int_{\mathcal{V}} \frac{\partial T}{\partial t}}_{TEND} = \underbrace{UT^*_{140E} + VT^*_{5S} - VT^*_{5N}}_{ADV_H} + \underbrace{WT^*_{-300m}}_{ADV_V} + MIX + \underbrace{\frac{1}{\rho C_p}\int_{\mathcal{A}} Q}_{SURF} \tag{5}$$

$$\underbrace{\int_{\mathcal{V}} \frac{\partial S}{\partial t}}_{TEND} = \underbrace{US^*_{140E} + VS^*_{5S} - VS^*_{5N}}_{ADV_H} + \underbrace{WS^*_{-300m}}_{ADV_V} + MIX + \underbrace{\int_{\mathcal{A}} F}_{SURF} \tag{6}$$

where $T^* \equiv T - T_{\text{ref}}$, $S^* \equiv S - S_{\text{ref}}$, $\mathcal{A}$ is the surface area, and MIX is the sum of diffusive and KPP terms. Nonlinear advection terms (such as UT, VT, and WT) are calculated, averaged, and saved during the model run.

The reference temperature and salinity are chosen as the average values in the analysis box during 2014–2018, $T_{\text{ref}} = 18.8°C$ and $S_{\text{ref}} = 35.0$, following the methodology of Kessler et al. (2019). Removing the reference values allows us to interpret the effects of advection at each face in terms of how they affect the mean properties in the box, rather than how much heat and salt goes through each face (Kessler et al., 2019; Lee et al., 2004); it does not affect the total advective divergence, only how it is split into horizontal and vertical components in the budgets.
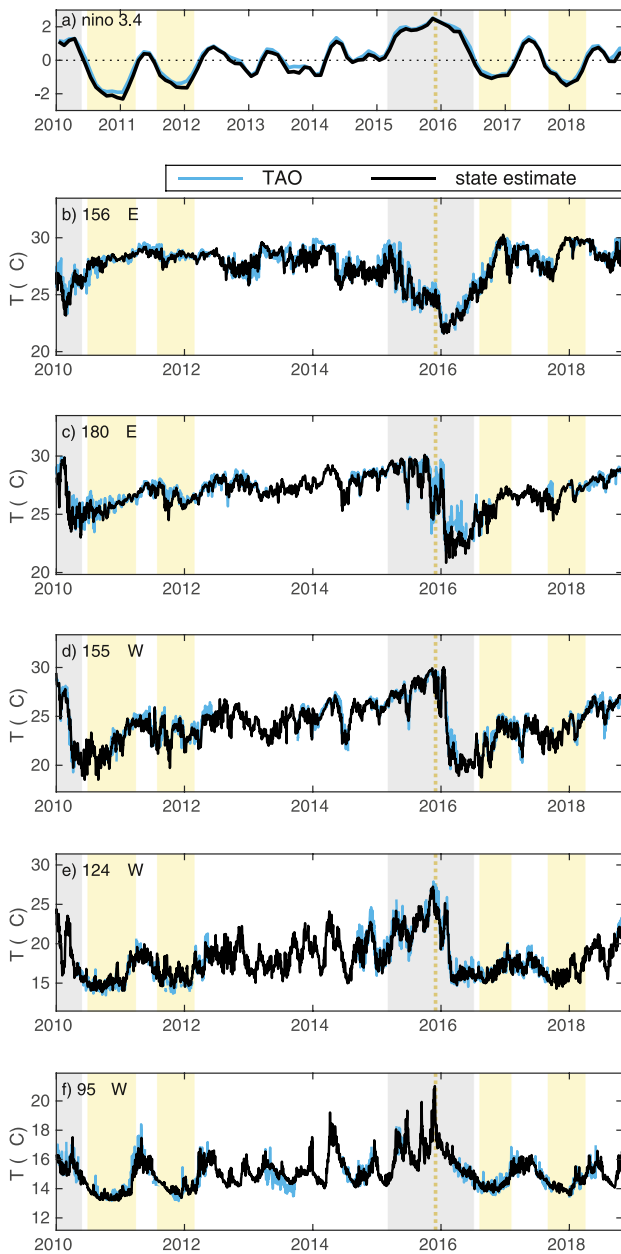
Figure 5. (a) Niño 3.4 index anomalies over the period 2010–2018 (blue) and calculated from the state estimate (black). (b–f) Daily averaged temperatures at 100 m in the state estimate (black) and TAO observations (blue) at five mooring locations on the equator with longitudes given in each panel. The five mooring locations are highlighted in Figure 1. Gray and yellow shading indicate periods when the Niño 3.4 anomaly is above 0.4 or below −0.4 for at least 6 months. Vertical dashed lines show the peak value in December 2015.

To focus on departures from normal conditions during El Niño, the month-by-month mean is removed from each budget term. The resulting budget anomalies are presented in Section 4. In the next section, we describe how an El Niño event affects the circulation and the upper-ocean temperature and salinity in TPOSE.

3. Diagnosing 2015/2016 El Niño Variability

Extending the 2010–2013 state estimate described in Verdy et al. (2017) through 2018 allows assessment of the 2015/2016 El Niño event. The state estimate reproduces the observed large-scale and mesoscale variability such as tropical instability waves (Verdy et al., 2017). As an example, we compare TPOSE temperature at 100 m to TAO moorings observations (Figure 5) which were not used in the data assimilation process, providing an independent validation of the product. In Figure 5a, the Niño3.4 index is compared with its model equivalent; the similarity gives confidence that the state estimate is adequate for investigating ENSO variability. Figures 5b–5f show the agreement between model and TAO observations for the 9-year period at 5 moorings locations along the equator. For all equatorial moorings, between 72% and 92% of the total variance at 100 m depth is captured by the state estimate. The fit is even better when comparing the variance at timescales longer than 20 days, thus we hypothesize that the differences are largely due to a lack of assimilated observations at daily timescales (Verdy et al., 2017).

The time series in Figure 5 show a strong signature of the 2015/2016 El Niño event and hints of a redistribution of heat from the west to the east. In 2015, the 100 m temperature is falling in the western Pacific (156°E) and rising in the central (155°W, 124°W) and eastern (95°W) parts of the basin. Then, in early 2016, there is an abrupt temperature drop in the central Pacific, followed by slower warming in the west and cooling in the east. Drivers of these signals are analyzed in Section 4.

Basin-averaged properties are compared to the gridded Argo product (Roemmich & Gilson, 2009) in Figure 6. Temperature, salinity, and the depth of the $\sigma_\theta = 25$ kg m^{-3} isopycnal are averaged inside the analysis box, that is, the top 300 m between 5°S and 5°N, east of 140°E. Note that the $\sigma_\theta = 25$ isopycnal is always contained within that box, reaching a maximum depth of 225 m over all grid points during 2010–2018. The evolution of the signals is plotted for the period 2014–2018, which is the focus of our analysis. The onset of the El Niño event is marked by a strong freshening and slight warming of the upper ocean, while the recovery is dominated by a sharp cooling and shoaling of the isopycnal. The recovery signal following the event persists into 2017 for salinity and σ_θ, and into 2018 for temperature. These signals are large enough to impact global averages of heat content anomalies (Roemmich et al., 2015).

WWV is not shown here but its variability follows that of the mean temperature (correlation coefficient = 0.96). As seen in Figure 6, upper ocean temperatures rise before and during the El Niño onset year, thus recharging the WWV; the abrupt cooling reflects the discharge of WWV as warm surface water is exported out of the equatorial region. The export of water with $\sigma_\theta < 25$ during December 2015–May 2016 is estimated to average about 40 Sv in the state estimate. This is primarily driven by anomalous ageostrophic transport at 5°N, as will be shown in Section 4.3.

WWV variability is analyzed by Huguenin et al. (2020); their Figure 3 shows WWV rising during the first 7 months of an El Niño, and then dropping, starting at about 11 months, by 5 times the amount of the rise, which
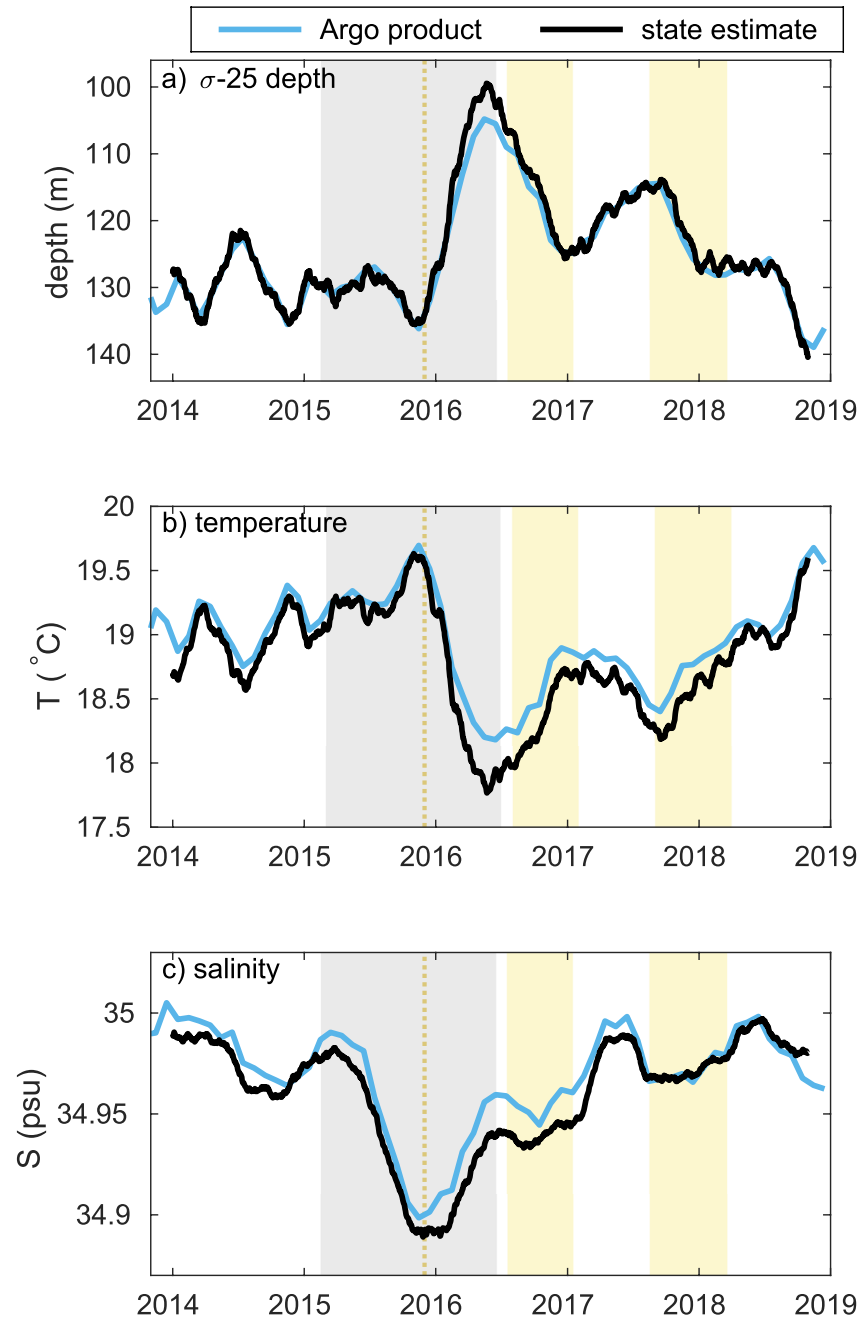
Figure 6. (a) Depth of the σ-25 isopycnal, (b) average temperature in the top 300 m and (c) average salinity in the top 300 m in the region 5°S–5°N, east of 140°E. Daily averages in the state estimate (black) are compared to the monthly Argo mapped product (blue) by Roemmich and Gilson (2009). Shading as in Figure 5.

is similar to our Figure 6b. Their La Niña WWV evolution is more or less the negative of the El Niño, and our 2017–2018 La Niña behaves similarly. The La Niña in 2016 overlaps with the aftermath of the El Niño and cannot be compared to their isolated cases.

The average salinity has significantly different time behavior compared to temperature. During the onset of El Niño, the equatorial box experiences rapid freshening; this reflects the eastward displacement of the relatively fresh warm pool. In contrast, the recovery is slower than in the case of temperature. The salinity budget presented in Section 4.4 shows that it results mainly from a balance between precipitation and ageostrophic advection at 5°N.
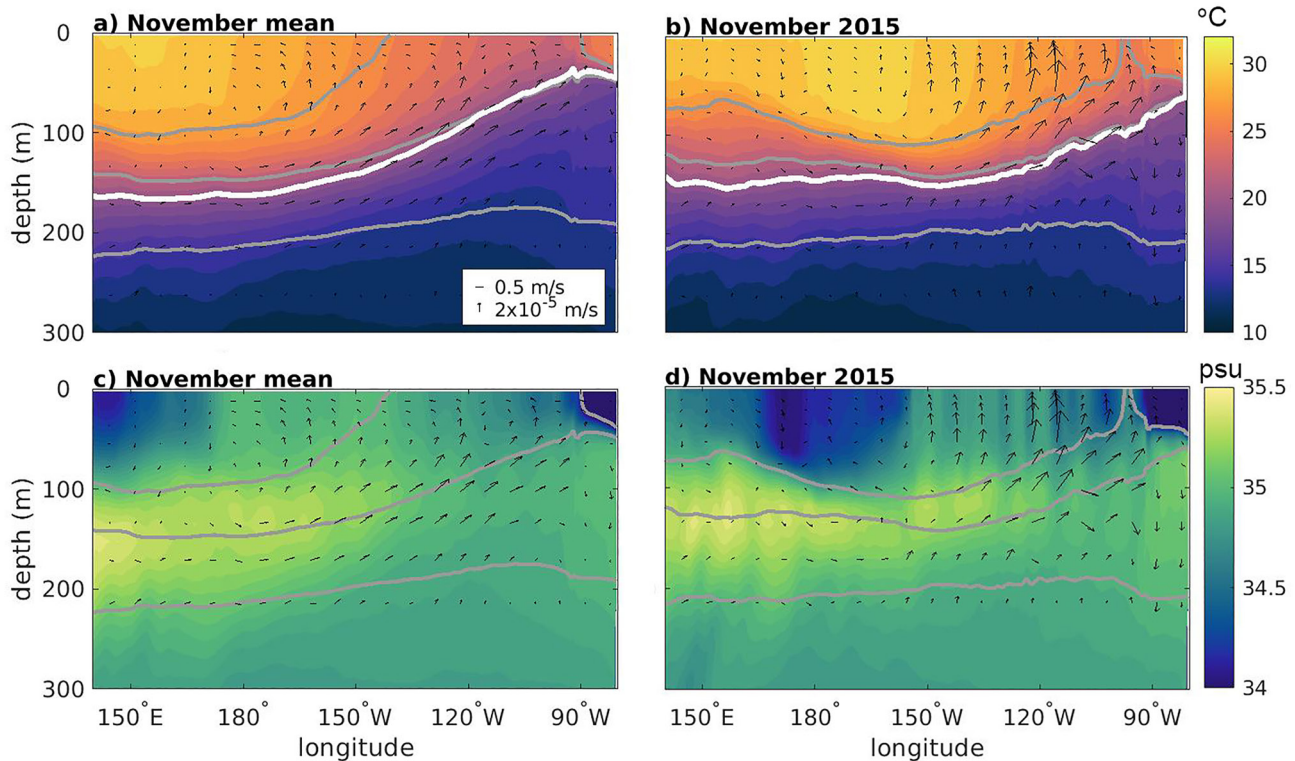
Figure 7. (a, b) Temperature and (c, d) salinity along the equator. Left column shows the November mean, right column shows November 2015. Gray contours indicate isopycnals (σ_θ = 1,023, 1,025, and 1,027 kg/m³); arrows represent zonal and vertical velocity. White contours highlight the 20°C isotherm.

Temperature and salinity along the equator are shown in Figures 7a and 7c for the 2014–2018 November average, and in Figures 4b and 4d for November 2015. We focus on the month of November as it marks the peak in the Niño 3.4 index (Figure 6a) and the regional heat content (Figure 6b). In the mean, there is a strong gradient from cold and fresh waters in the east to warm and salty in the west, with the exception of the surface fresh pool in the west. The gradients are intensified during the 2017 La Niña (not shown). In contrast, the November 2015 El Niño conditions indicate that surface warm-fresh waters have moved east, and the thermocline has shoaled in the west and deepened in the east as expected (Johnson et al., 2002). The warm pool now sits closer to the central Pacific, which is fresher due to the combined effects of zonal advection and the eastward shift of atmospheric convection and rain following the warm waters (Gasparin & Roemmich, 2016).

Velocity in a cross-equatorial section at 140°W is shown in Figure 8. The TPOSE 2014–2018 November mean currents (Figure 8a) compare qualitatively with the observations of Johnson et al. (2002), taken mostly during the 1990's (Figure 5c). Note that velocity observations are not assimilated in TPOSE. The Equatorial Undercurrent (EUC), centered at the equator and ~120 m, is weaker in the state estimate, as are the south and north branches of the westward South Equatorial Current (SEC) and the Tsuchiya jets. The shape and magnitude of the North Equatorial Counter Current (NECC) are similar to the observations, though centered slightly farther north at ~8°N. The tropical meridional overturning circulation seen in Figure 8a is the manifestation of poleward Ekman transport at the surface and equatorward geostrophic transport below (Perez & Kessler, 2009).

During the peak of El Niño (Figure 8b), the EUC is weakened compared to average conditions (Johnson et al., 2000, 2002). This is consistent with weakened trade winds and surface waters sloshing eastward (Figure 7), which relaxes the pressure gradient driving the undercurrent. As an index of the EUC strength, we consider the largest daily average eastward velocity in the range 3°S–3°N at 140°W (Figure 8d). This index shows that the undercurrent starts decaying around June 2015, remains weak through February 2016, and returns to full strength by April 2016. Since this is a propagating signal, the exact timing depends on the longitude considered.

In contrast, the NECC is stronger than average during El Niño, consistent with the observations of Taft and Kessler (1991). For an NECC index, we consider the largest daily average eastward velocity in the range
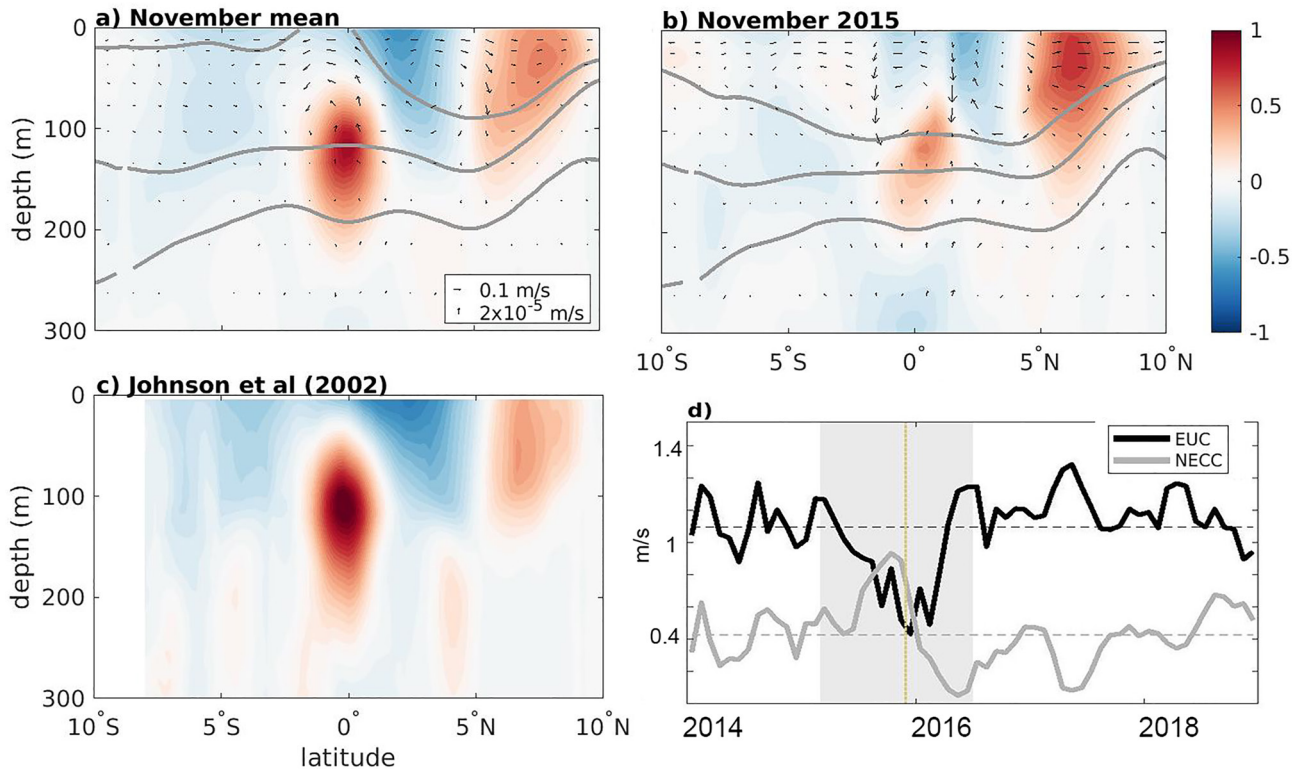
Figure 8. Velocity at 140°W in the state estimate: zonal component (colors); meridional and vertical components (arrows) in (a) the November average, (b) November 2015, and (c) observations by Johnson et al. (2002). Gray contours show isopycnals ($\sigma_\theta = 1{,}023$, $1{,}025$, and $1{,}027$ kg/m³). During the 2015 El Niño, the EUC weakens and the NECC strengthens. (d) Indices for the EUC (black) and the NECC (gray) in the state estimate; see text for details. Dashed lines indicate the mean.

3°N–10°N at 170°W (Figure 8d). Anomalous downwelling on both sides of the equator is seen in November 2015, and the meridional overturning cells are weakened.

4. Budget Analysis

We consider budgets in the top 300 m of the region between 5°S and 5°N and east of 140°E. The mean balances are schematized in Figure 9; transport through each face of the box is quantified from the 2014–2018 TPOSE solution (temperature and salinity budget diagnostic terms were not archived in the initial 2010–2013 TPOSE product and, since our focus is on the El Niño event, we opted for saving computer resources instead of generating them). Tendency terms averaged over the 5-year period are negligible. Horizontal transport is separated into ageostrophic (including Ekman) and geostrophic components at the west, south, and north faces. Geostrophic transport is calculated from the pressure gradients and tracer values at each boundary, in a way that is consistent with the advection scheme used in the MITgcm. Ageostrophic transport is simply the residual between total and geostrophic transports.

4.1. Mean Budgets

Figure 9 shows the mean budget terms (numbers in bold face) and their standard deviation, calculated from daily averages. In some cases the variability far exceeds the mean, as is the case for geostrophic volume transport at 140°E. The variability is discussed in the next subsections.

The mean circulation in a meridional section averaged between 140°E and the South American continent consists of equatorial upwelling and poleward Ekman transport near the surface, with downwelling around ±5° and deeper equatorward transport to close the overturning circulation (see vector plot on Figure 9a). Vertical advection brings water into the box and meridional Ekman advection carries it out. The northward geostrophic flow at 5°S is opposite in direction and larger in magnitude compared to the ageostrophic flow, due to strong geostrophic
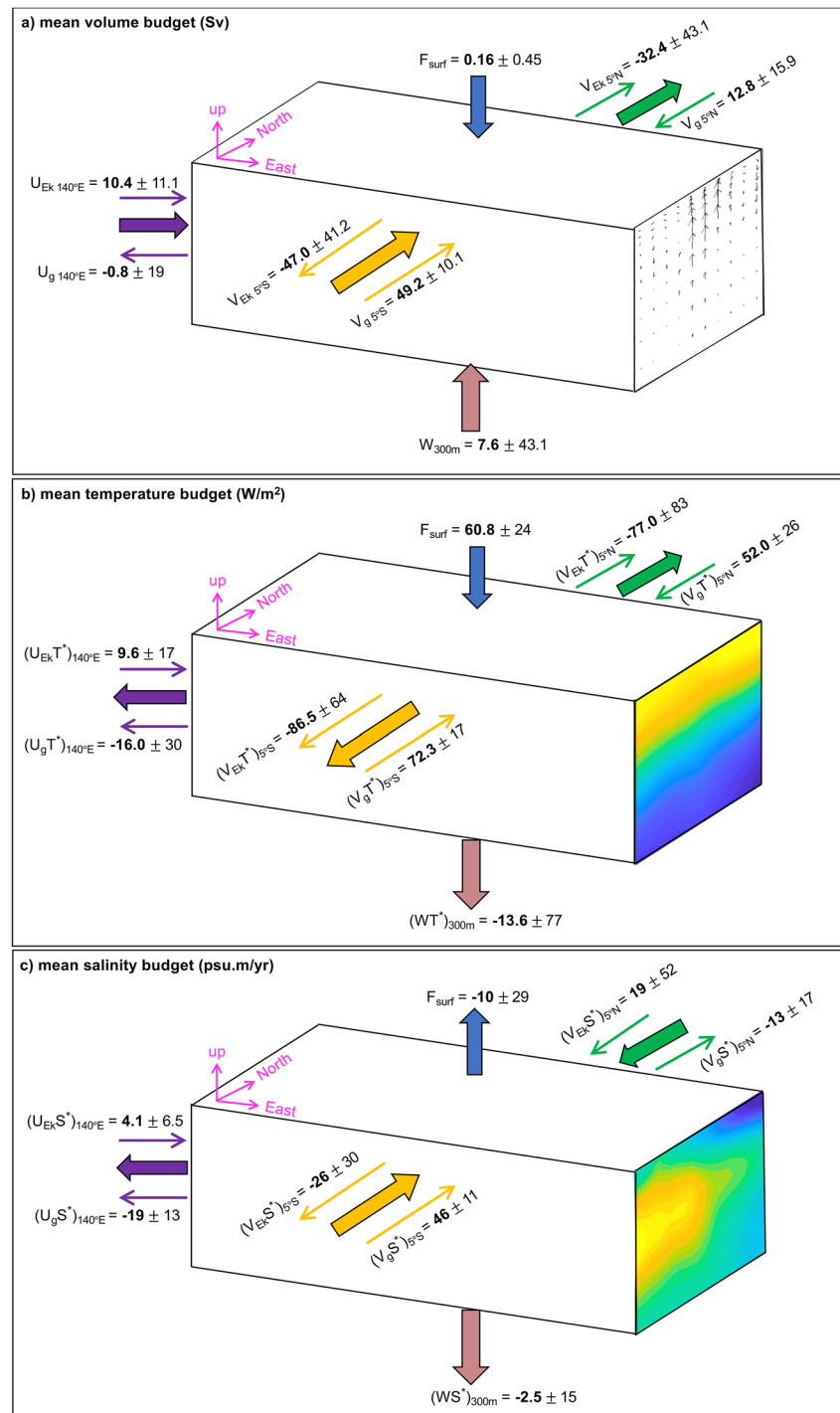
Figure 9. Mean budgets in the analysis box, expressed as transport through each face; the means and standard deviations are listed in the figure. The color of the arrows is consistent with the colors in Figures 10, 12, and 13 for surface forcing (blue), vertical advection (pink), and advection through the west face (purple), south face (orange), and north face (green). The eastern boundary is closed by land. (a) Volume transport (in Sv); horizontal transport is decomposed into geostrophic and ageostrophic contributions. Black arrows on the East face show the zonally averaged meanmeridional and vertical circulation inside the box. (b) Temperature transport (in °C/yr); vertical and horizontal transport is defined as in Equation 2, with $T^* = T - T_{ref}$. Colored contours on the East face show the zonally averaged meantemperature. (c) Salinity transport (in psu/yr), with $S^* = S - S_{ref}$. Colored contours on the East face show the zonally averaged meansalinity.

western boundary currents near the maritime continent. The zonal flow coming in from the west face is predominantly ageostrophic; the geostrophic westward boundary current along Papua New Guinea is largely compensated by the eastward EUC and NECC. There is a small input of water at the surface from precipitation. The northward transport at 5°N is the only net sink in the volume budget, balancing sources at the top, bottom, west and south faces.

In the temperature budget (Figure 9b), the surface flux is a major source of heat. It is balanced by cooling due to upwelling and to advection of warm surface water out of the box at the west, south and north faces. At 5°S, the geostrophic flow is mostly deeper than the Ekman flow and as a result does not carry as much heat. At 140°E, shallow westward geostrophic flow contributes to significant heat transport, even though the net geostrophic flow through the face is small.

Horizontal advection is the dominant term in the salinity budget (Figure 9c). Because of the subsurface salinity maximum south of the equator, the positive (northward) geostrophic transport exceeds the negative Ekman transport at 5°S. In contrast, the low salinity at 5°N ($S < S_{\text{ref}}$) leads to negative geostrophic transport and positive Ekman transport. The geostrophic transport at 140°E is a net sink, as are surface forcing and upwelling.

The remainder of the analysis focuses on the time variability of the budgets, after the mean and seasonal cycle are removed. Because the daily budget terms are noisy, we apply a 30-day running mean for better visualization of the balances at play. First we examine the volume budget, which has direct implications for the transport of heat and salt. We then analyze the temperature and salinity budgets to document the mechanisms responsible for the regional cooling and freshening during El Niño and the subsequent recovery to baseline conditions.

4.2. Volume Budget Variability

In the regional volume budget, there is an approximate balance between horizontal advection, vertical advection, and (a small contribution) surface forcing. The tendency term integrated over the region is negligible. Figure 10a shows the anomalies, defined as deviations from the seasonally varying mean, for each of these terms. Their cumulative mean is shown in Figure 10b. From the cumulative plots we infer that in 2015 there is positive anomalous horizontal transport and negative anomalous vertical transport. These are the result of weakened winds, which slow down the shallow overturning circulation (zonal winds control the Ekman transport and the wind stress curl affects the geostrophic flow; e.g., Capontondi et al., 2005). There is also a small positive surface flux in late 2015 as a result of enhanced precipitation.

Horizontal advection can be decomposed into transport through the west (140°E), south (5°S) and north (5°N) faces of the analysis box (Figures 7c and 7d). Prior to the El Niño event, the enhanced horizontal transport into the domain resulted from enhanced flow through the western side, partially compensated by reduced transport through the south face. During the El Niño, the export of water through the northern side is the dominant signal, peaking in February 2016.

Further decomposing horizontal advection into geostrophic and ageostrophic transport provides insight into the El Niño dynamical response (Figures 10e–10h). This highlights the balance between the geostrophic and Ekman transport anomalies at 5°N throughout 2015, presumably because winds are weaker than average (geostrophic transport is less positive and ageostrophic is less negative than average). This lasts until early 2016 when the trade winds strengthen rapidly and strong Ekman export abruptly breaks the balance. In the south, there is also a weakening of geostrophic transport in 2015, compensated by an increase in Ekman transport in late 2015/early 2016, followed by a slow return to normal. The anomalous transport through 140°E is mostly geostrophic and characterized by an increase in eastward flow in the top 100 m around 3°N.

The sensitivity of the volume budget to the choice of north and south boundaries was assessed by varying the width of the region over which transport is calculated (Figure 11). There are high correlations between the transport at 5°N and the transport at 3°N ($\rho = 0.77$) and at 9.5°N ($\rho = 0.74$). Correlations are even higher between the transport at 5°S and the transport at 3°S ($\rho = 0.94$) and 9.5°S ($\rho = 0.84$). At 140°E, the transport integrated between 5°S and 5°N is highly correlated with the transport integrated between 9.5°S and 9.5°N ($\rho = 0.83$). The correlation is lower with transport integrated between 3°S and 3°N ($\rho = 0.65$), as expected since the smaller domain misses part of the shallow overturning circulation, which closes around ±5°. Overall, these results give us confidence that our analysis is not highly sensitive to the choice of bounding latitudes.
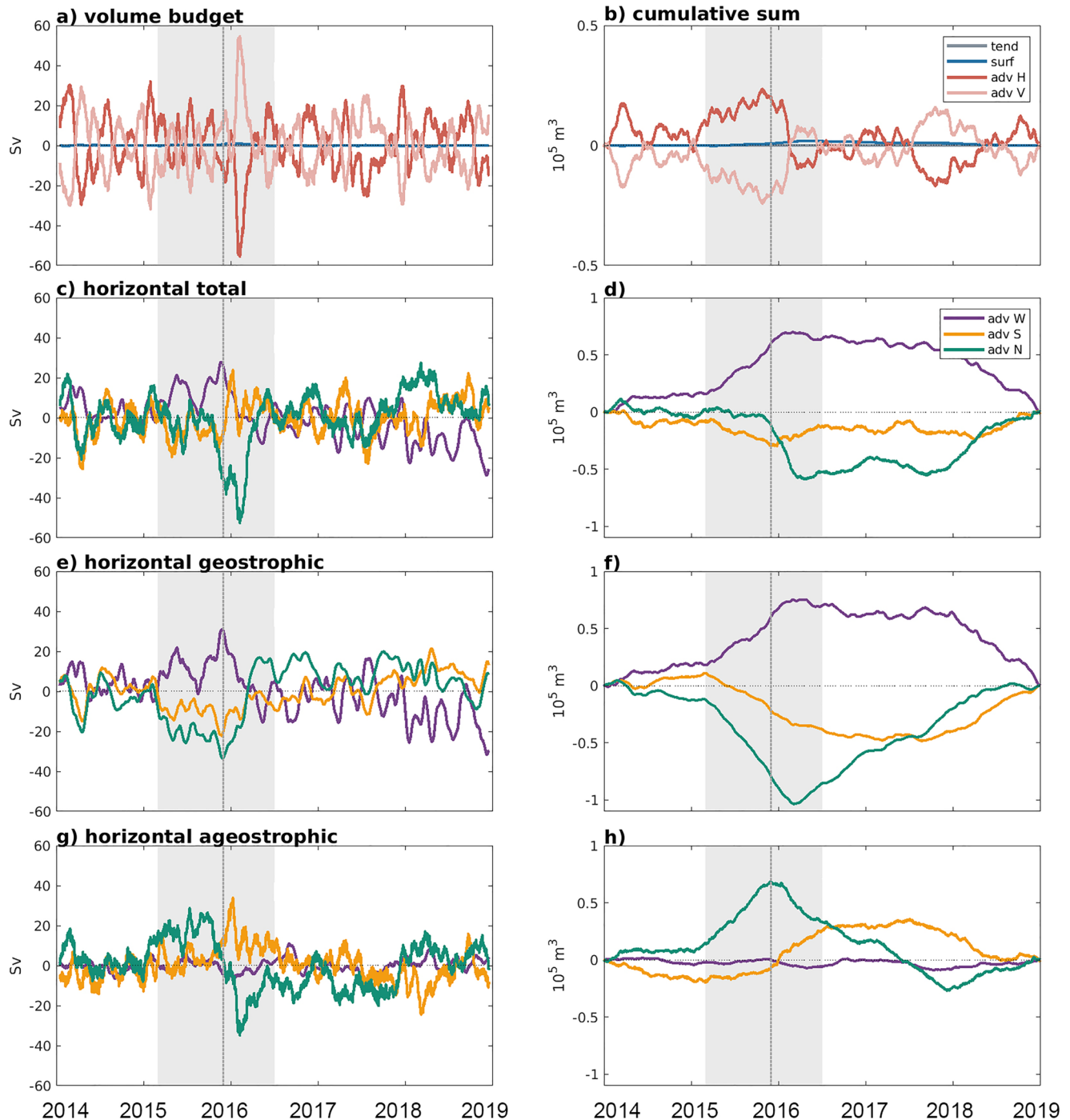
Figure 10. Volume budget terms after removing the seasonally varying mean. Left column: time series smoothed with a 30-day running average. Right column: cumulative sum. (a, b) Contributions from surface fluxes (blue), horizontal advection (red), vertical advection (pink), and the resulting tendency (gray). (c, d) Horizontal advection through each face of the analysis domain: 140°E (purple), 5°S (orange), and 5°N (green). (e, f) Geostrophic component. (g, h) Ageostrophic component (including Ekman). The 2015/2016 El Niño period is shaded gray, with a vertical line separating the onset from the recovery.

4.3. Temperature Budget Variability

Temperature budget term anomalies are plotted in Figure 12 and their statistics are given in Table 1. The average tendency over the box (gray curve) is the result of a balance between advection and surface forcing. Because we integrate down to 300 m which is well below the mixed layer, the contribution of mixing from below is
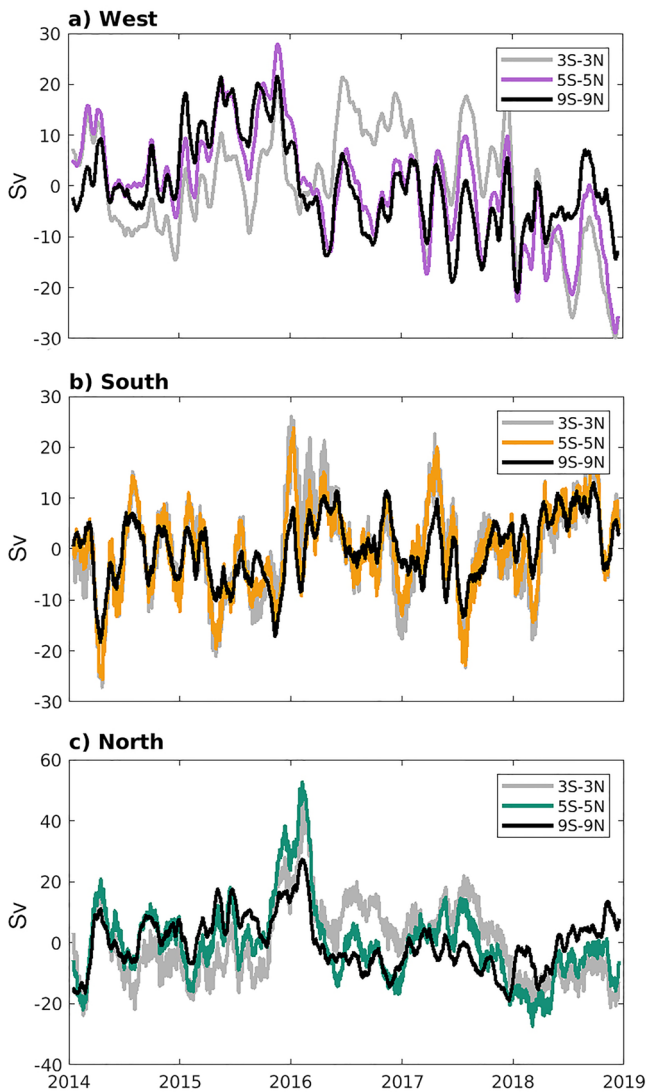
Figure 11. Horizontal transport at (a) 140°E, (b) South face, and (c) North face for different choice of the box over which the analysis is performed: 3°S–3°N (gray), 5°S–5°N (colors as in Figure 9), 9.5°S–9.5°N (black).

negligible (Table 1). The cumulative sum of the tendency term (gray curve in Figure 12b) is equivalent to the anomaly of the average temperature time series shown Figure 6b. Time-integrating the budget terms this way helps understand the regional temperature evolution.

It is immediately apparent in Figure 12 that horizontal advection plays a significant role in explaining the cooling during the 2015 El Niño. Enhanced surface cooling throughout 2015 is largely balanced by horizontal and vertical advection bringing heat into the region. The positive temperature transport anomaly at 140°E is due to anomalous eastward geostrophic flow in the west (Figures 10e and 10f) acting on the positive temperature gradient, causing the warm pool to move eastward into the tropical Pacific domain. At the end of El Niño, warm surface water is exported north by Ekman flow as the westerly winds recover their strength. Cooling also results from vertical transport at 300 m. This vertical transport across 300 m may be largely adiabatic, as the flow follows isopycnals that slope upward (Figure 7).

Horizontal temperature transport at each face (Figures 12c and 12d) follows closely the patterns in the volume budget (Figures 10c and 10d), which implies that the anomalous temperature transport is strongly linked to the anomalous flow. This is confirmed when temperature transport anomalies $(UT)'$ are decomposed into anomalous advection of mean temperature, $U'\bar{T}$, and mean advection of temperature anomalies, $\bar{U}T'$ (not shown). Between 87% and 95% of the temperature transport is explained by the anomalous advection of mean temperature (highest value for northern face transport, lowest value for western face), compared to 0%–12% for the mean advection of temperature anomalies and 0%–6% for the residual (anomalous advection of temperature anomalies). Therefore, the analysis of the geostrophic and ageostrophic volume transport presented in the previous subsection also informs the temperature transport variability.

The average values of budget term anomalies during the periods of El Niño onset (March–November 2015) and recovery (December 2015–June 2016) are listed in Table 1. Surface heat flux anomaly is dominant during the onset, exceeding the standard deviation of the budget term. During the recovery, horizontal advection is dominant, especially the ageostrophic contribution at 5°N.

4.4. Salinity Budget Variability

Salinity tendency is driven primarily by horizontal advection and surface fluxes (Figures 13a and 13b). Vertical advection plays a small role in the variability of regional salinity. Horizontal advection brings in freshwater during most of 2015. During the El Niño, the center of atmospheric convection moves off the maritime continent and over the Pacific and, combined with reduced evaporation under weaker winds, the enhanced precipitation leads to the freshening of the Central Pacific region from boreal spring 2015 into 2016.

Horizontal advection changes in late 2015 and is responsible for the El Niño recovery. Decomposing the advective components (Figures 13c and 13d) shows that the freshening during the 2015 El Niño comes from the west and south faces. In late 2015, there is strong advection of fresh water to the north resulting in the recovery from El Niño conditions. Like with temperature, this is associated with Ekman advection of surface waters. Unlike temperature, however, the salinity transport at 5°N is attributed to both the advection of anomalous salinity gradients (59%–71% of the variance explained) and the anomalous advection of the mean gradient (0%–48% of the variance explained).

Average values of the budget terms during the El Niño onset and recovery (Table 1) show the dominance of surface freshwater flux during the onset and horizontal advection during the recovery.
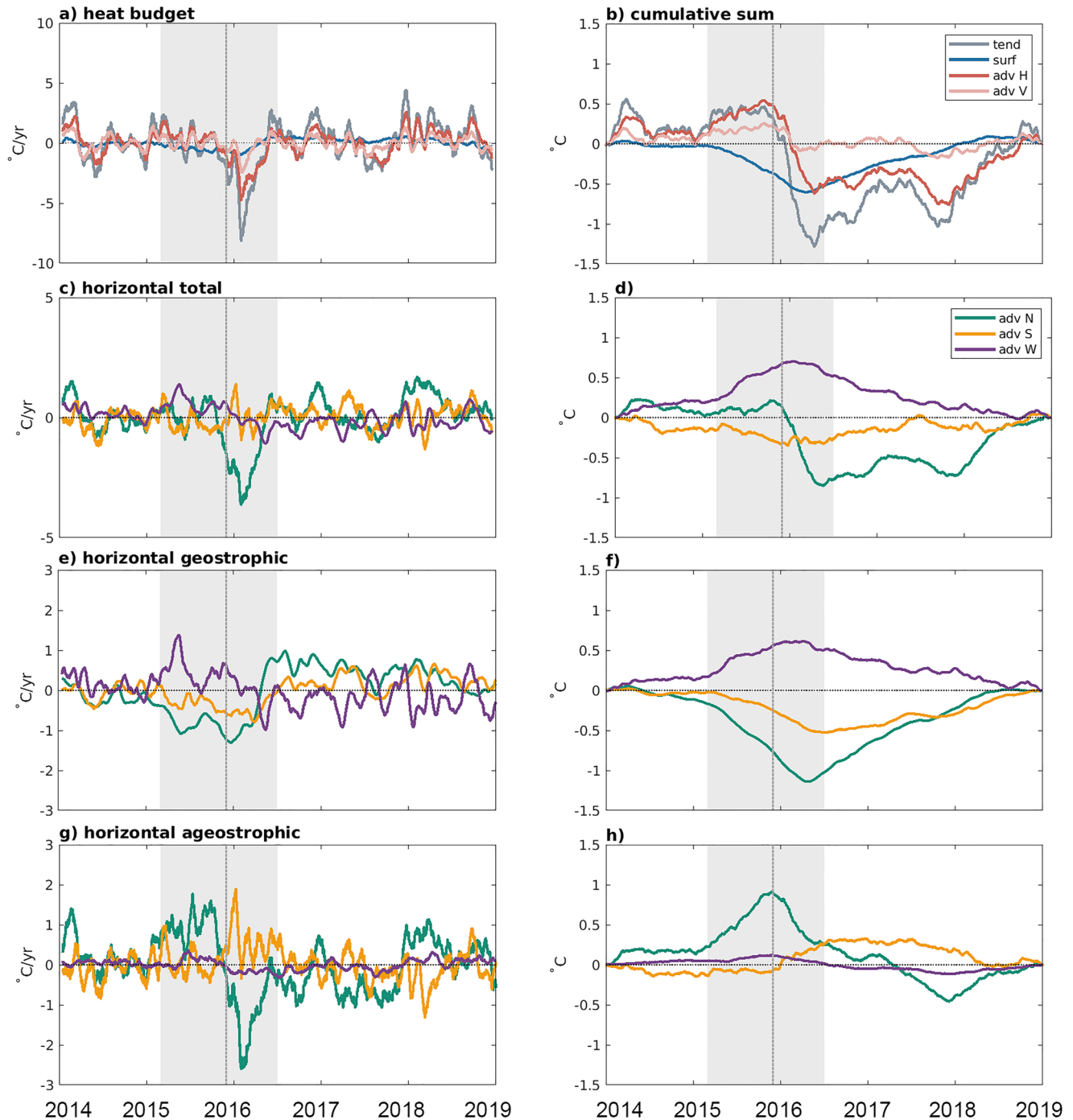
Figure 12. Temperature budget terms, as in Figure 10.

5. Discussion

Having quantified the basin-scale budgets in TPOSE from 2014 through 2018, it is now appropriate to put these results in the context of the observational based analysis from Kessler et al. (2019) and other previous works. The meridional heat transport divergence between 9.5°S and 9.5°N observed by Kessler et al. (2019) has an annual mean value of −0.03°C/month, resulting from partial compensation between Ekman (−0.12°C/month) and geostrophic (0.09°C/month) components. The TPOSE 2010–2018 mean meridional transport divergence between those same latitudes (9.5°S–9.5°N) is approximately −0.06°C/month, which is notably different from

Table 1
Budget Anomalies: Standard Deviation of Daily Averaged Budget Terms and Mean Values During El Niño Onset (March–November 2015) and Recovery (December 2015–June 2016)

Budget term	Temperature (°C/yr)			Salinity (10^{-2} psu/yr)		
	Std. dev.	Onset	Recovery	Std. dev.	Onset	Recovery
Tendency	3.64	0.15	−2.30	16.6	−9.2	5.9
Surface	0.44	−0.46	−0.27	7.4	−7.8	−7.0
Mixing	0.0078	−0.011	0.0065	0.062	0.081	0.030
Vertical advection	1.73	0.16	−0.31	4.3	0.48	−0.32
Horizontal advection	2.14	0.48	−1.69	16.8	−2.1	13.2
140°E Ageostrophic	0.39	0.09	−0.17	1.9	0.51	0.35
Geostrophic	0.65	0.51	−0.09	3.6	−2.1	3.4
5°N Ageostrophic	1.54	0.90	−1.10	13.6	0.21	17.0
Geostrophic	0.59	−0.80	−0.44	5.4	2.3	−7.8
5°S Ageostrophic	1.37	0.08	0.58	8.8	1.5	4.7
Geostrophic	0.36	−0.30	−0.47	3.5	−4.5	−4.5

Note. Horizontal advection terms are defined as positive when into the analysis box.

the observed value, though the glider data is from a different time period (2008–2015) that includes anomalously weak divergence in 2008 and 2009 and excludes the strong El Niño signal. In our analysis domain, which has a narrower latitudinal definition (5°S–5°N), the net meridional transport divergence is −0.08°C/month. Consistent with observations, it results from Ekman divergence (−0.35°C/month) exceeding geostrophic convergence (0.27°C/month). Across the southern boundary of the analysis domain at 9.5°S, Kessler et al. (2019) find that western boundary current advection of heat through the Solomon Sea is a large signal that is strongly correlated with the Niño 3.4 index but is largely canceled out by geostrophic advection in the interior of the basin. At 5°S in TPOSE, we similarly find that the geostrophic Solomon Sea heat transport is opposite in sign and similar in magnitude to the geostrophic heat transport east of the Solomon Islands (i.e., east of 155°E), though the Solomon Sea transport is only half the magnitude of the interior transport. Thus, the total geostrophic flow across 5°S contributes to a net export of heat from the equatorial strip, and that signal is strong following the 2015/2016 El Niño. The Ekman transport integrated over 5°S is generally weak.

The story is quite different at 5°N, where Ekman transport plays a leading role in the budgets. Izumo (2005) also notes this strong asymmetry and low correlation between surface meridional transports at 5°N and 5°S. The winds at 5°N experience a much stronger deviation from mean conditions in 2015/2016 than at 5°S (Figure 14). The onset of El Niño comes with weakened winds, collapsing the shallow meridional overturning circulation, and the reduction in poleward Ekman transport causes the equatorial temperature to rise. When the winds intensify again, the Ekman export of heat is highly efficient at removing the heat that has accumulated in the equatorial region. The compensating geostrophic branch of the overturning cell lags the Ekman branch, causing a net volume divergence in the region and shoaling of the σ_{25} isopycnal.

In addition to the weakening of the overturning, the western warm/fresh pool moves east into the central Pacific during the onset of El Niño. This brings anomalous heat and freshwater into our analysis box. The strong freshwater anomaly of 2015 is documented in Gasparin and Roemmich (2016) and attributed to changes in the zonal wind stress and pressure gradient fluctuations (Gasparin & Roemmich, 2017).

Surface fluxes and wind-driven lateral transport are also identified as the leading drivers of WWV variability in the modeling study by Huguenin et al. (2020). This is not surprising, since WWV is highly correlated with the upper 300-m mean temperature. Their idealized El Niño WWV budget analysis highlights the two phases of WWV discharge, which is defined as the period over which WWV decreases and starts approximately 5 months before the peak of El Niño in their simulation. In our temperature budget, the mean temperature doesn't start dropping until about 1 month before the peak; however cooling through surface fluxes begins right at the onset of El Niño (Figure 12). Surface fluxes and vertical mixing anomalies drive the first phase of the discharge, which
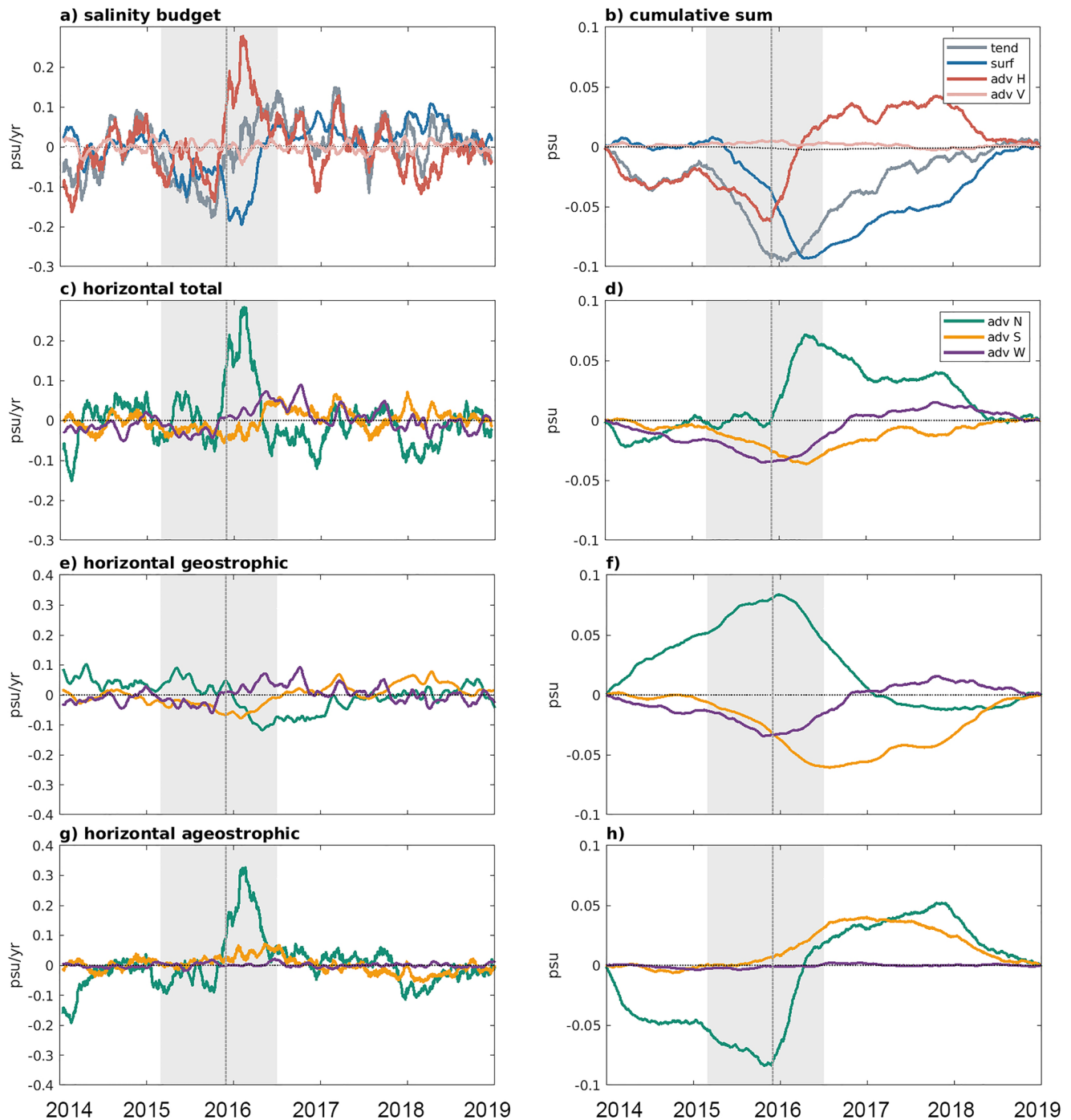
Figure 13. Salinity budget terms, as in Figure 12.

lasts about 7 months (Huguenin et al., 2020). The second phase is dominated by lateral transport across 5°N and 5°S and the Indonesian Throughflow and starts a month before the niño3.4 peak (Huguenin et al., 2020). This is consistent with our results, showing cooling through horizontal advection starting in October 2015. However in our case the lateral advection has decayed by April 2016, whereas theirs lasts for about 12 months.

There are limitations to the present study. For one, the primary signals discussed here are lateral transports. Vertical exchanges do matter, as we quantify in our analysis. However, our analysis box has a fixed depth, and thus these terms include both cross-isopycnal and along-isopycnal transports. Kessler et al. (2019) found that
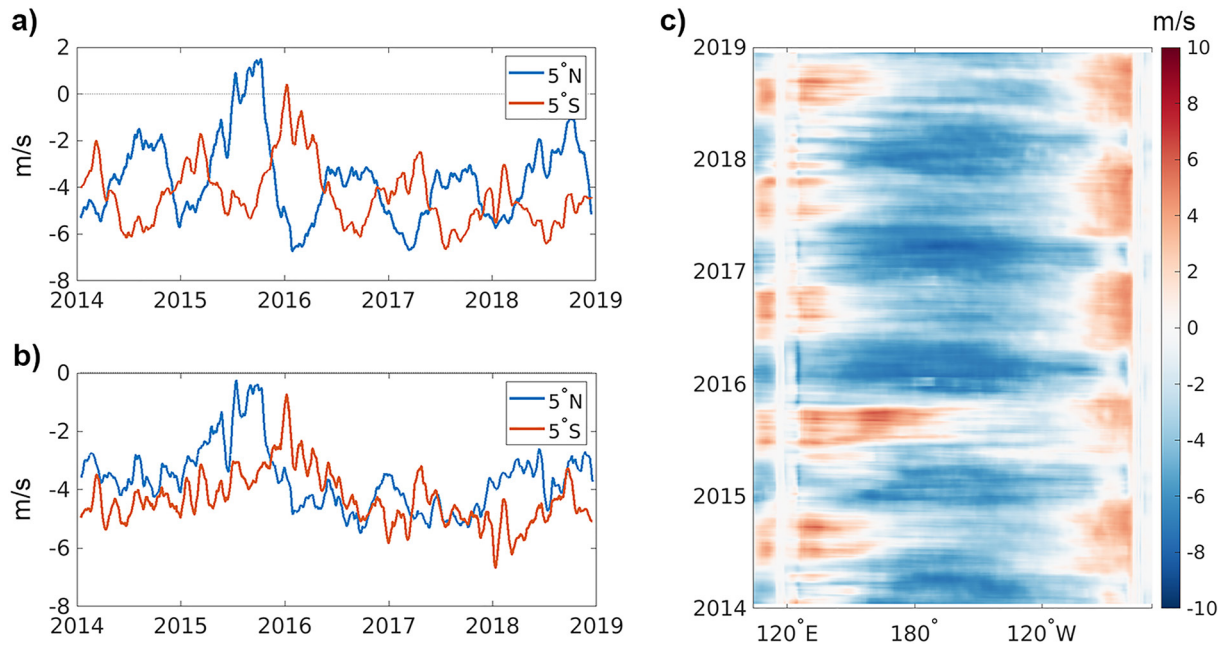
Figure 14. (a) Zonal wind speed at 5°S and 5°N between 150°E and 250°E; (b) seasonal cycle removed. (c) Zonal winds at 5°N, with a 30 days running mean.

estimating interannual variability in temperature horizontal advection by integrating over the top 500 m gave equivalent results to those derived using an isopycnal bottom (e.g., $\sigma_\theta = 26.9$, which has a mean depth of 450 m in TPOSE). Nevertheless, it is worth further exploring the partitioning of the vertical flow by considering a domain that follows isopycnals (as in Kessler et al. (2019)) or isotherms (as in Deppenmeier et al. (2021)).

Additionally, a caveat of the model setup is that the Indonesian Throughflow (ITF) is prescribed through the open boundary conditions. Those are not adjusted in our data assimilation. The model does perform poorly compared to observations in the maritime continent due to its complex topography and shallow regions. For these reasons, we are not assimilating observations in the maritime continent, and have placed the edge of our analysis box far enough east that it does not directly include the ITF. That being said, transport at the western wall of our box is bound to be influenced by the ITF variability. As can be seen from Figures 12d and 13d, transport at 140°E is an important term in the temperature and salinity budgets, steadily bringing anomalously warm and fresh water into the tropical Pacific throughout 2014 and 2015. Anomalous ITF heat transport is linked to the "failure" of the anticipated El Niño in 2014 and the development of a particularly strong event in 2015 (Mayer & Balmaseda, 2021; Mayer et al., 2018).

The most significant limitation of this study is that it analyzes a single El Niño event; therefore we cannot generalize our results or comment on differences between El Niño types. Argo profiling floats are a primary constraint for TPOSE; because of the relatively recent nature of the data set, there is a limit on how far back we can meaningfully perform the data assimilation. However, the extension of TPOSE back to the beginning of 2009 is underway, which will resolve the 2009–2010 El Niño. Repeating the budgets analyses presented in this study will allow us to investigate the relative importance of the different processes and how transport varies during East-Pacific and Central-Pacific El Niño events.

6. Summary and Concluding Remarks

We have produced an ocean state estimate that is consistent with model dynamics and observations from the TPOS, making the product useful for analyzing the ocean variability through the 2015/2016 El Niño event and addressing the Wyrtki challenge. The model links the forcing to the observations, creating Kelvin and Rossby waves forced by the winds in the Equatorial waveguide and observed by the TAO/TRITON array. Using this state estimate, we diagnose the mean state and budgets during 2014–2018, then contrast the 2015/2016 El Niño conditions to that baseline.

ENSO-related changes in the tropical Pacific ocean heat content, as well as lateral and vertical redistribution of heat within the upper ocean, are thoroughly documented (Cheng et al., 2019). The present study provides a link to the mechanisms driving the heat (and salt) exchanges in and out of a box-shaped domain the central-East equatorial Pacific. Wind-driven horizontal circulation changes, together with surface fluxes, are found to be the dominant mechanisms during the onset and recovery of the 2015/2016 El Niño. The ocean response to wind changes has implications for OHT (Ferrari & Ferreira, 2011) and, although much of the heat is internally redistributed within the wider Pacific basin (Forget & Ferreira, 2019), the modulation of local air-sea fluxes impacts the effective OHT at higher latitudes.

The mean equatorial Pacific ocean state is governed by shallow meridional overturning cells and air-sea exchanges (Figure 9). Quantifying the TPOSE budgets shows that changes in meridional transport drive variability in the upper ocean temperature and salinity between 5°S and 5°N, though vertical advection and surface fluxes also play important roles. The importance of Ekman and geostrophic meridional currents in observed ocean temperature is discussed by Kessler et al. (2019), who find that the net meridional transport is strongly correlated with the temperature tendency and with the Niño 3.4 index. Similarly, Li et al. (2022) discuss the link between net meridional transport and WWV using a global ocean reanalysis. Our results quantifying the importance of the meridional transport to the temperature budget are consistent with both these papers.

Meridional heat advection strongly varies longitudinally (Li et al., 2022). Future studies may aim at contrasting heat and freshwater budgets in different parts of the equatorial Pacific, such as the Eastern Edge of the Warm Pool (EEWP) or the Pacific Upwelling Mixing Physics (PUMP) regions. Mixed layer heat budgets can be useful for a wide range of applications, from estimating effective diffusivity coefficients (Cronin et al., 2015) to understanding coral bleaching (Qiu et al., 2021). Salinity budgets, while less commonly used, can help quantify factors influencing tropical dynamics, such as barrier layer formation. TPOSE has been useful for understanding the large-scale budgets and addressing the Wyrtki challenge; further TPOSE analyses can shed light on some of these above-mentioned topics. Increasing vertical resolution in future state estimates will be key to resolving small-scale upper ocean processes.

Data Availability Statement

The state estimate used in this work was produced using the open-source MIT general circulation model (https://github.com/MITgcm/MITgcm) and the TAF commercial product (http://www.fastopt.com/products/taf/taf.shtml). Model input files are available at https://doi.org/10.5281/zenodo.7869465 (Verdy, 2023). The TPOSE output is freely available online at http://www.ecco.ucsd.edu/tpose.html. Model output was analyzed and plotted using the commercial software Matlab (https://www.mathworks.com/products/matlab.html). Codes used for offline budget calculations are available at https://doi.org/10.5281/zenodo.7869465 (Verdy, 2023). Data sets used for assimilation are referenced in Section 2.1 and are made freely accessible online by the TAO Project Office of NOAA/PMEL (http://www.pmel.noaa.gov/tao), the World Ocean Database accessed from the National Centers for Environmental Information (https://www.ncei.noaa.gov), and the Radar Altimeter Database System (http://rads.tudelft.nl/rads/rads.shtml). Microwave OI SST data are produced by Remote Sensing Systems and sponsored by National Oceanographic Partnership Program (NOPP) and the NASA Earth Science Physical Oceanography Program; data are available at https://www.remss.com. Argo data (Argo, 2000) were collected and made freely available by the International Argo Program and the national programs that contribute to it (https://argo.ucsd.edu, https://www.ocean-ops.org). The Argo Program is part of the Global Ocean Observing System. The ECCOv4r4 product is freely available online (ECCO consortium et al., 2021). Computational resources are provided by the San Diego Supercomputer Center Triton Shared Computing Cluster at the University of California, San Diego (https://doi.org/10.57873/T34W2R).

References

Argo (2000). Argo float data and metadata from global data assembly centre (Argo GDAC) [Dataset]. SEANOE. https://doi.org/10.17882/42182

Boyer, T., Baranova, O., Coleman, C., Garcia, H., Grodsky, A., Locarnini, R., et al. (2018). World ocean database 2018. In A. V. Mishonov, & Technical (Eds.), *NOAA atlas NESDIS* (Vol. 87).

Capotondi, A., Alexander, M. A., Deser, C., & McPhaden, M. J. (2005). Anatomy and decadal evolution of the Pacific subtropical–Tropical Cells (STCs). *Journal of Climate*, *18*(18), 3739–3758. https://doi.org/10.1175/JCLI3496.1

Cheng, L., Trenberth, K. E., Fasullo, J. T., Mayer, M., Balmaseda, M., & Zhu, J. (2019). Evolution of ocean heat content related to ENSO. *Journal of Climate*, *32*(12), 3529–3556. https://doi.org/10.1175/JCLI-D-18-0607.1

Cravatte, S., Kessler, W. S., Smith, N., & Wijffels, S. E. (2016). First report of TPOS 2020. GOOS-215, 200. Retrieved from http://tpos2020.org/first-report/

Cronin, M. F., Pelland, N. A., Emerson, S. R., & Crawford, W. R. (2015). Estimating diffusivity from the mixed layer heat and salt balances in the North Pacific. *Journal of Geophysical Research: Oceans*, *120*(11), 7346–7362. https://doi.org/10.1002/2015JC011010

Dee, D. P., Uppala, S. M., Simmons, A. J., Berrisford, P., Poli, P., Kobayashi, S., et al. (2011). The ERA-interim reanalysis: Configuration and performance of the data assimilation system. *Quarterly Journal of the Royal Meteorological Society*, *137*(656), 553–597. https://doi.org/10.1002/qj.828

Deppenmeier, A. L., Bryan, F. O., Kessler, W. S., & Thompson, L. (2021). Modulation of cross-isothermal velocities with ENSO in the tropical Pacific cold tongue. *Journal of Physical Oceanography*, *51*(5), 1559–1574. https://doi.org/10.1175/jpo-d-20-0217.1

ECCO Consortium, Fukumori, I., Wang, O., Fenty, I., Forget, G., Heimbach, P., & Ponte, R. M. (2021). ECCO ancillary data (version 4 release 4) [Dataset]. NASA Physical Oceanography DAAC. https://doi.org/10.5067/ECCL4-ANC44

Ferrari, R., & Ferreira, D. (2011). What processes drive the ocean heat transport? *Ocean Modelling*, *38*(3–4), 171–186. https://doi.org/10.1016/j.ocemod.2011.02.013

Forget, G., Campin, J.-M., Heimbach, P., Hill, C. N., Ponte, R. M., & Wunsch, C. (2015). ECCO version 4: An integrated framework for non-linear inverse modeling and global ocean state estimation. *Geoscientific Model Development*, *8*(10), 3071–3104. https://doi.org/10.5194/gmd-8-3071-2015

Forget, G., & Ferreira, D. (2019). Global ocean heat transport dominated by heat export from the tropical Pacific. *Nature Geoscience*, *12*(5), 12351–12354. https://doi.org/10.1038/s41561-019-0333-7

Gasparin, F., & Roemmich, D. (2016). The strong freshwater anomaly during the onset of the 2015/2016 El Niño. *Geophysical Research Letters*, *43*(12), 6452–6460. https://doi.org/10.1002/2016GL069542

Gasparin, F., & Roemmich, D. (2017). The seasonal march of the equatorial Pacific upper-ocean and its El Niño variability. *Progress in Oceanography*, *156*, 1–16. https://doi.org/10.1016/j.pocean.2017.05.010

Guan, C. Y., Wang, X., & Yang, H. J. (2023). Understanding the development of the 2018/2019 central Pacific El Niño. *Advances in Atmospheric Sciences*, *40*(1), 177–185. https://doi.org/10.1007/s00376-022-1410-1

Hersbach, H., Bell, B., Berrisford, P., Biavati, G., Horányi, A., Muñoz Sabater, J., et al. (2018). ERA5 hourly data on single levels from 1979 to present. *Copernicus Climate Change Service (C3S) Climate Data Store (CDS)*. https://doi.org/10.24381/cds.adbb2d47

Huguenin, M. F., Holmes, R. M., & England, M. H. (2020). Key role of diabatic processes in regulating warm water volume variability over ENSO events. *Journal of Climate*, *33*(22), 9945–9964. https://doi.org/10.1175/JCLI-D-20-0198.1

Izumo, T. (2005). The equatorial undercurrent, meridional overturning circulation, and their roles in mass and heat exchanges during El Niño events in the tropical Pacific Ocean. *Ocean Dynamics*, *55*(2), 110–112. https://doi.org/10.1007/s10236-005-0115-1

Johnson, G. C., Mcphaden, M. J., & Firing, E. (2001). Equatorial Pacific Ocean horizontal velocity, divergence, and upwelling. *Journal of Physical Oceanography*, *31*(3), 839–849. https://doi.org/10.1175/1520-0485(2001)031<0839:epohvd>2.0.co;2

Johnson, G. C., McPhaden, M. J., Rowe, G. D., & McTaggart, K. E. (2000). Upper equatorial Pacific Ocean current and salinity variability during the 1996–1998 El Nino–La Nina cycle. *Journal of Geophysical Research*, *105*(C1), 1037–1053. https://doi.org/10.1029/1999jc900280

Johnson, G. C., Sloyan, B. M., Kessler, W. S., & McTaggart, K. E. (2002). Direct measurements of upper ocean currents and water properties across the tropical Pacific during the 1990s. *Progress in Oceanography*, *52*(1), 31–61. https://doi.org/10.1016/S0079-6611(02)00021-6

Kessler, W. S., Hristova, H. G., & Davis, R. E. (2019). Equatorward western boundary transport from the South Pacific: Glider observations, dynamics and consequences. *Progress in Oceanography*, *175*, 208–225. https://doi.org/10.1016/j.pocean.2019.04.005

Kim, S. T., Yu, J. Y., & Lu, M. M. (2012). The distinct behaviors of Pacific and Indian Ocean warm pool properties on seasonal and interannual time scales. *Journal of Geophysical Research*, *117*(D5), D05128. https://doi.org/10.1029/2011JD016557

Large, W., McWilliams, J., & Doney, S. (1994). Ocean vertical mixing: A review and a model with a nonlocal boundary layer parameterization. *Reviews of Geophysics*, *32*(4), 363–403. https://doi.org/10.1029/94rg01872

Large, W. G., & Yeager, S. G. (2009). The global climatology of an interannually varying air-sea flux data set. *Climate Dynamics*, *33*(2–3), 341–364. https://doi.org/10.1007/s00382-008-0441-3

Lee, T., Fukumori, I., & Tang, B. (2004). Temperature advection: Internal versus external processes. *Journal of Physical Oceanography*, *34*(8), 1936–1944. https://doi.org/10.1175/1520-0485(2004)034<1936:TAIVEP>2.0.CO;2

L'Heureux, M. L., Takahashi, K., Watkins, A. B., Barnston, A. G., Becker, E. J., Di Liberto, T. E., et al. (2017). Observing and predicting the 2015/2016 El Niño. *Bulletin of the American Meteorological Society*, *98*(7), 1363–1382. https://doi.org/10.1175/BAMS-D-16-0009.1

Li, X., Hu, Z.-Z., Huang, B., & Jin, F.-F. (2022). Oceanic meridional transports and their roles in warm water volume variability and ENSO in the tropical Pacific. *Climate Dynamics*, *59*(1–2), 245–262. https://doi.org/10.1007/s00382-021-06124w

Marshall, J., Adcroft, A., Hill, C., Perelman, L., & Heisey, C. (1997). A finite-volume, incompressible Navier Stokes model for studies of the ocean on parallel computers. *Journal of Geophysical Research*, *102*(C3), 5753–5766. https://doi.org/10.1029/96jc02775

Mayer, M., & Balmaseda, M. A. (2021). Indian Ocean impact on ENSO evolution 2014–2016 in a set of seasonal forecasting experiments. *Climate Dynamics*, *56*(7–8), 2631–2649. https://doi.org/10.1007/s00382-020-05607-6

Mayer, M., Balmaseda, M. A., & Haimberger, L. (2018). Unprecedented 2015/2016 Indo-Pacific heat transfer speeds up tropical Pacific heat recharge. *Geophysical Research Letters*, *45*(7), 3274–3284. https://doi.org/10.1002/2018GL077106

McDougall, T. J. (2003). Potential enthalpy: A conservative oceanic variable for evaluating heat content and heat fluxes. *Journal of Physical Oceanography*, *33*(5), 945–963. https://doi.org/10.1175/1520-0485(2003)033<0945:PEACOV>2.0.CO;2

McPhaden, M. J., Zebiak, S. E., & Glantz, M. H. (2006). ENSO as an integrating concept in Earth science. *Science*, *314*(5806), 1740–1745. https://doi.org/10.1126/science.1132588

Meinen, C. S., & McPhaden, M. J. (2000). Observations of warm water volume changes in the equatorial Pacific and their relationship to El Niño and La Niña. *Journal of Climate*, *13*(20), 3551–3559. https://doi.org/10.1175/1520-0442(2000)013<3551:oowwvc>2.0.co;2

Penny, S. G., Akella, S., Balmaseda, M. A., Browne, P., Carton, J. A., Chevallier, M., et al. (2019). Observational needs for improving ocean and coupled reanalysis, S2S prediction, and decadal prediction. *Frontiers in Marine Science*, *6*, 391. https://doi.org/10.3389/fmars.2019.00391

Perez, W. S., & Kessler, R. C. (2009). Three-dimensional structure of tropical cells in the central equatorial Pacific Ocean. *Journal of Physical Oceanography*, *39*(1), 27–49. https://doi.org/10.1175/2008jpo4029.1

Piecuch, C. G. (2017). A note on practical evaluation of budgets in ECCO version 4 release 3. Retrieved from http://hdl.handle.net/1721.1/111094

Qiu, B., Colin, P. L., & Chen, S. (2021). Time-varying upper ocean circulation and control of coral bleaching in the western tropical Pacific. *Geophysical Research Letters*, *48*(14), e2021GL093632. https://doi.org/10.1029/2021GL093632

Roberts, C. D., Palmer, M. D., Allan, R. P., Desbruyeres, D., Hyder, P., Liu, C., & Smith, D. (2017). Surface flux and ocean heat transport convergence contributions to seasonal and interannual variations of ocean heat content. *Journal of Geophysical Research: Oceans*, *122*(1), 726–744. https://doi.org/10.1002/2016JC012278

Roemmich, D., Church, J., Gilson, J., D, D. M., Sutton, P., & Wijffels, S. (2015). Unabated planetary warming and its ocean structure since 2006. *Nature Climate Change*, *5*(3), 240–245. https://doi.org/10.1038/nclimate2513

Roemmich, D., & Gilson, J. (2009). The 2004-2008 mean and annual cycle of temperature, salinity, and steric height in the global ocean from the Argo program. *Progress in Oceanography*, *82*(2), 81–100. https://doi.org/10.1016/j.pocean.2009.03.004

Santoso, A., Mcphaden, M. J., & Cai, W. (2017). The defining characteristics of ENSO extremes and the strong 2015/2016 El Niño. *Reviews of Geophysics*, *55*(4), 1079–1129. https://doi.org/10.1002/2017RG000560

Scharroo, R., Leuliette, E. W., Lillibridge, J. L., Byrne, D., Naeije, M. C., & Mitchum, G. T. (2013). RADS: Consistent multi-mission products. In *Proceedings of the symposium on 20 years of progress in radar altimetry* (p. 4). European Space Agency. ESA SP-710.

Song, L., Li, Y., Wang, J., Wang, F., Hu, S., Liu, C., et al. (2018). Tropical meridional overturning circulation observed by subsurface moorings in the western Pacific. *Scientific Reports*, *8*(1), 7632. https://doi.org/10.1038/s41598-018-26047-7

Taft, B. A., & Kessler, W. S. (1991). Variations of zonal currents in the central tropical Pacific during 1970 to 1987: Sea level and dynamic height measurements. *Journal of Geophysical Research*, *96*(C7), 12599–12618. https://doi.org/10.1029/91jc00781

Verdy, A. (2023). Tpose configuration and analysis files [Dataset]. Zenodo. https://doi.org/10.5281/zenodo.7869465

Verdy, A., Cornuelle, B. D., Mazloff, M. R., & Rudnick, D. L. (2017). Estimation of the tropical Pacific Ocean state 2010-2013. *Journal of Atmospheric and Oceanic Technology*, *34*(7), 1501–1517. https://doi.org/10.1175/jtech-d-16-0223.1

Wang, X., Guan, C., Huang, R. X., Tan, W., & Wang, L. (2019). The roles of tropical and subtropical wind stress anomalies in the El Niño Modoki onset. *Climate Dynamics*, *52*(11), 6585–6597. https://doi.org/10.1007/s00382-018-4534-3

Wunsch, C., & Heimbach, P. (2013). Dynamically and kinematically consistent global ocean circulation and ice state estimates. In G. Siedler, S. M. Griffies, J. Gould, & J. A. Church (Eds.), *Ocean circulation and climate: A 21st century perspective*, *International geophysics series* (2nd ed., Vol. 103, pp. 553–558). Elsevier. https://doi.org/10.1016/B978-0-12-391851-2.00021-0

Wyrtki, K. (1981). An estimate of equatorial upwelling in the Pacific. *Journal of Physical Oceanography*, *11*(9), 1205–1214. https://doi.org/10.1175/1520-0485(1981)011<1205:aeoeui>2.0.co;2

Xie, R., & Fang, X. (2020). The unusual 2014–2016 El Niño events: Dynamics, prediction and enlightenments. *Science China Earth Sciences*, *63*(5), 626–633. https://doi.org/10.1007/s11430-019-9561-2